

High-Performance Statistical Computing in the Computing Environments of the 2020s

Seyoon Ko, Hua Zhou, Jin Zhou, and Joong-Ho Won

Department of Statistics, Seoul National University, Seoul, Korea

Department of Biostatistics, UCLA Fielding School of Public Health, Los Angeles, CA, USA

Department of Epidemiology and Biostatistics, College of Public Health, University of Arizona, Tucson, AZ, USA

Department of Statistics, Seoul National University, Seoul, Korea, e-mail: wonj@stats.snu.ac.kr

Abstract: Technological advances in the past decade, hardware and software alike, have made access to high-performance computing (HPC) easier than ever. We review these advances from a statistical computing perspective. Cloud computing allows access to supercomputers affordable. Deep learning software libraries make programming statistical algorithms easy, and enable users to write code once and run it anywhere from a laptop to a workstation with multiple graphics processing units (GPUs) or a supercomputer in a cloud. To promote statisticians to benefit from these developments, we review recent optimization algorithms that are useful for high-dimensional models and can harness the power of HPC. Code snippets are provided for the readers to grasp the ease of programming. We also provide an easy-to-use distributed matrix data structure suitable for HPC. Employing this data structure, we illustrate various statistical applications including large-scale nonnegative matrix factorization, positron emission tomography, multidimensional scaling, and ℓ_1 -regularized Cox regression. Our examples easily scale up to an 8-GPU workstation and a 720-CPU-core cluster in a cloud. As a case in point, we analyze the on-set of type-2 diabetes from the UK Biobank with 200,000 subjects and about 500,000 single nucleotide polymorphisms using the HPC ℓ_1 -regularized Cox regression. Fitting a half-million-variate model takes less than 45 minutes, reconfirming known associations. To our knowledge, the feasibility of jointly genome-wide association analysis of survival outcomes at this scale is first demonstrated.

Keywords and phrases: high-performance statistical computing, cloud computing, MM algorithms, PDHG, multidimensional scaling, nonnegative matrix factorization, PET imaging, Cox regression.

1. Introduction

Clock speeds of the central processing units (CPUs) on the desktop and laptop computers hit the physical limit more than a decade ago, and there will be likely no major breakthrough until quantum computing becomes practical. Instead, the increase in computing power is now accomplished by using multiple cores within a processor chip. High-performance computing (HPC) means computations that are so large that their requirement on storage, main memory, and raw computational speed cannot be met by a single (desktop) computer (Hager and Wellein, 2010). Modern HPC machines are equipped with more than one CPU that can work on the same problem (Eijkhout, 2016). Often, special-purpose co-processors such as graphical processing units (GPUs) are attached to the CPU for order-of-magnitudes of acceleration for some tasks. A GPU can be thought of a massively parallel matrix-vector multiplier and vector transformer on a data stream. With the needs of analyzing terabyte- or even petabyte-scale data common, the success of large-scale statistical computing heavily relies on how to engage HPC in the statistical practice.

About a decade ago, the second author discussed the potential of GPUs in statistical computing. Zhou et al. (2010) predicted that GPUs will fundamentally alter the landscape of computational statistics. Yet, it does not appear that GPU computing, or HPC in general, has completely smeared into the statistical community. Part of the reasons for this may be attributed to the fear that parallel and distributed code is difficult to program, especially in R (R Core Team, 2018), the programming language of statisticians. On the other hand, the landscape of scientific computing in general, including so-called data science (Donoho, 2017), has indeed substantially changed. Many high-level programming languages, e.g., Python (van Rossum, 1995) and Julia (Bezanson et al., 2017), support parallel computing by design or through standard libraries. Accordingly, many software tools have been developed in order to ease programming in and managing HPC environments. Last but not least, cloud computing (Fox, 2011) is getting rid of the necessity for purchasing expensive supercomputers and scales computation as needed.

Concurrently, easily parallelizable algorithms for fitting statistical models with hundreds of thousand parameters have also seen significant advances. Traditional Newton-Raphson or quasi-Newton type of algorithms face two major challenges in contemporary problems: 1) explosion of dimensionality renders storing and inversion of Hessian matrices prohibitive; 2) regularization of model complexity is almost essential in high-dimensional settings, which is often realized by nondifferentiable penalties; this leads to high-dimensional, nonsmooth optimization problems. For these reasons, nonsmooth first-order methods have been extensively studied during the past decade (Beck, 2017). For relatively simple, decomposable penalties (Negahban et al., 2012), the proximal gradient method (Beck and Teboulle, 2009; Combettes and Pesquet, 2011; Parikh and Boyd, 2014; Polson et al., 2015) produces a family of easily parallelizable algorithms. For the prominent example of the Lasso (Tibshirani, 1996), this method contrasts to the highly efficient sequential coordinate descent method of Friedman et al. (2010) and the smooth approximation approaches, e.g., Hunter and Li (2005). Decomposability or separability of variables is often the key to parallel and distributed algorithms. The popular alternating direction method of multipliers (ADMM, Gabay and Mercier, 1976; Glowinski and Marroco, 1975; Boyd et al., 2010) achieves this goal through variable splitting, while often resulting in nontrivial subproblems to solve. As an alternative, the primal-dual hybrid gradient (PDHG) algorithm (Zhu and Chan, 2008; Esser et al., 2010; Chambolle and Pock, 2011; Condat, 2013; Vũ, 2013) has a very low per-iteration complexity, useful for complex penalties such as the generalized lasso (Tibshirani and Taylor, 2011; Ko et al., 2019+; Ko and Won, 2019). Another route toward separability is through the MM principle (Lange et al., 2000; Hunter and Lange, 2004; Lange, 2016), which has been explored in Zhou et al. (2010). In fact, the proximal gradient method can be viewed as a realization of the MM principle. Recent developments in the application of this principle include distance majorization (Chi et al., 2014) and proximal distance algorithms (Keys et al., 2019).

The goal of this paper is to review the advances in parallel and distributed computing environments during the last decade and demonstrate how easy it has become to write a code for large-scale, high-dimensional statistical models and run it on various distributed environments. In order to make the contrast clear, we deliberately take examples from Zhou et al. (2010), namely nonnegative matrix factorization (NMF), positron emission tomography (PET), and multidimensional scaling (MDS). The difference lies in the scale of the examples: our experiments deal with data of size at least $10,000 \times 10,000$ and as large as $200,000 \times 200,000$ for dense data, and $810,000 \times 179,700$ for sparse data. This contrasts with the size of at best 4096×2016 of Zhou et al. (2010). This level of scaling is possible because the use of *multiple* GPUs in a distributed fashion has become handy, as opposed to the single GPU, CUDA C implementation of 2010. Furthermore, using the power of cloud computing and modern deep learning software, we show that exactly the *same* code can run on multiple

CPU cores and/or clusters of workstations. Thus we bust the common misconception that deep learning software is dedicated to neural networks and heuristic model fitting. Wherever possible, we apply more recent algorithms in order to cope with the scale of the problems. In addition, a new example of large-scale proportional hazards regression model is investigated. We demonstrate the potential of our approach through a single multivariate Cox regression model regularized by the ℓ_1 penalty on the UK Biobank genomics data (with 200,000 subjects), featuring time-to-onset of Type 2 Diabetes (T2D) as outcome and 500,000 genomic loci harboring single nucleotide polymorphisms as covariates. To our knowledge, such a large-scale joint genome-wide association analysis has not been attempted. The reported Cox regression model retains a large proportion of *bona fide* genomic loci associated with T2D and recovers many loci near genes involved in insulin resistance and inflammation, which may have been missed in conventional univariate analysis with moderate statistical significance values.

The rest of this article is organized as follows. We review HPC systems and see how they have become easy to use in Section 2. In Section 3, we review software libraries employing the “write once, run everywhere” principle (especially deep learning software), and discuss how they can be employed for fitting high-dimensional statistical models on the HPC systems of Section 2. In Section 4, we review modern scalable optimization techniques that suit well to the HPC environment. We present how to distribute a large matrix over multiple devices in Section 5, and numerical examples of NMF, PET, MDS, and ℓ_1 -regularized Cox regression in Section 6. Finally, we conclude the article in Section 7.

2. Accessible High-Performance Computing Systems

2.1. Preliminaries

Since modern HPC relies on parallel computing, in this section we review several concepts from parallel computing literature at a level minimally necessary for the subsequent discussions. Further details can be found in Nakano (2012); Eijkhout (2016).

Data parallelism. While parallelism can appear at various levels such as instruction-level and task-level, what is most relevant to statistical computing is data-level parallelism or data parallelism. If data can be split into several chunks that can be processed independently of each other, then we say there is data parallelism in the problem. Many operations such as scalar multiplication of a vector, matrix-vector multiplication, and summation of all elements in a vector can exploit data parallelism using parallel architectures discussed shortly.

Memory models. In any computing system, processors (CPUs or GPUs) need to access data residing in the memory. While *physical* computer memory uses complex hierarchies (L1, L2, and L3 caches; bus- and network-connected, etc.), systems employ abstraction to provide programmers an appearance of transparent memory access. Such *logical* memory models can be categorized into the shared memory model and the distributed memory model. In the shared memory model, all processors share the *address space* of the system’s memory even if it is physically distributed. For example, if two processors refer to a variable x , that means the variable is stored in the same memory address; if a processor alters the variable, then the other processor is affected by the changed value. Modern CPUs that have several cores within a processor chip fall into this category. On the other hand, in the distributed memory model, the system has memory both physically and logically distributed. Processors have their own memory address spaces, and cannot see each other’s memory directly. If two processors refer

to a variable x , then there are two separate memory locations, each of which belongs to each processor under the same name. Hence the memory does appear distributed to programmers, and the only way processors can exchange information with each other is through passing data through some explicit communication mechanism. The advantage at the cost of this complication is scalability — the number of processors that can work in a tightly coupled fashion is much greater in distributed memory systems (say 100,000) than shared memory systems (say four). Hybrids of the two memory models are also possible. A typical computer *cluster* consists of multiple *nodes* interconnected in a variety of network topology. A node is a workstation that can run standalone, with its main memory shared by several processors installed on the motherboard. Hence within a node, it is a shared memory system, whereas across the nodes the cluster is a distributed memory system.

Parallel programming models. For shared-memory systems, programming models based on *threads* are most popular. A thread is a stream of machine language instructions that can be created and run in parallel during the execution of a single program. OpenMP is a widely used extension to the C and Fortran programming languages based on threads. It achieves data parallelism by letting the compiler know what part of the sequential program is parallelizable by creating multiple threads. Simply put, each processor core can run a thread operating on a different partition of the data. In distributed-memory systems, parallelism is difficult to achieve via a simple modification of sequential code like by using OpenMP. The programmer needs to coordinate communications between processors not sharing memory. A de facto standard for such processor-to-processor communication is the message passing interface (MPI). MPI routines mainly consist of *point-to-point communication calls* that send and receive data between two processors, and *collective communication calls* that all processors in a group participate in. Typical collective communication calls include

- Scatter: one processor has data as an array, and each other processor receives a partition of the array;
- Gather: one processor collects data from all other processors to construct an array;
- Broadcast: one processor sends its data to all other devices;
- Reduce: gather data and produce a combined output based on an associative binary operator, such as sum or maximum of all the elements.

Parallel architectures. To realize the above models, a computer architecture that allows simultaneous execution of multiple machine language instructions is required. A single instruction, multiple data (SIMD) architecture has multiple processors that execute the same instruction on different parts of the data. The GPU falls into this category of architectures, as its massive number of cores can run a large number of threads that share memory. A multiple instruction, multiple data (MIMD), or single program, multiple data (SPMD) architecture has multiple CPUs that execute independent parts of program instructions on their own data partition. Most computer clusters fall into this category.

2.2. Multiple CPU nodes: clusters, supercomputers, and clouds

Computing on multiple nodes can be utilized in many different scales. For mid-sized data, one may build his/her own cluster with a few nodes. This requires determining the topology and purchasing all the required hardware, along with resources to maintain it. This is certainly not familiar to virtually all statisticians. Another option may be using a well-maintained supercomputer in a nearby HPC center. A user can take advantage of the facility with up to hundreds of thousand cores. The computing jobs on these facilities are often controlled by a

job scheduler, such as Sun Grid Engine (Gentzsch, 2001), Slurm (Yoo et al., 2003), Torque (Staples, 2006), etc. However, access to supercomputers is almost always limited. (Can you name a “nearby” HPC center from your work? If so, how can you submit your job request? What is the cost?) Even when the user has access to them, he/she often has to wait in a very long queue until the requested computation job is started by the scheduler.

In recent years, cloud computing has emerged as a third option. It refers to both the applications delivered as services over the Internet and the hardware and systems software in the data centers that provide those services (Armbrust et al., 2010). Big information technology companies such as Amazon, Microsoft, and Google lend their practically infinite computing resources to users on demand by wrapping the resources as “virtual machines”, which are charged per CPU hours and storage. Users basically pay utility bills for their use of computing resources. An important implication of this infrastructure to end-users is that the cost of using 1000 virtual machines for one hour is almost the same as using a single virtual machine for 1000 hours. Therefore a user can build his/her own virtual cluster “on the fly,” increasing the size of the cluster as the size of the problem to solve grows. A catch here is that a cluster does not necessarily possess the power of HPC as suggested in Section 2.1: a requirement for high performance is that all the machines should run in tight lockstep when working on a problem (Fox, 2011). However, early cloud services were more focused on web applications that do not involve frequent data transmissions between computing instances, and less optimized for HPC, yielding discouraging results (Evangelinos and Hill, 2008; Walker, 2008).

Eventually, many improvements have been made at hardware and software levels to make HPC on clouds feasible. At hardware level, cloud service providers now support CPU instances such as *c4*, *c5*, and *c5n* instances of Amazon Web Services (AWS), with up to 48 physical cores of higher clock speed of up to 3.4 GHz along with support for accelerated SIMD computation. If network bandwidth is critical, the user may choose instances with faster networking (such as *c5n* instances in AWS), allowing up to 100 Gbps of network bandwidth. At the software level, these providers support tools that manage resources efficiently for scientific computing applications, such as ParallelCluster (Amazon Web Services, n.d.) and ElastiCluster (University of Zurich, n.d.). These tools are designed to run programs in clouds in a similar manner to proprietary clusters through a job scheduler. In contrast to a physical cluster in an HPC center, a virtual cluster on a cloud is exclusively created for the user; there is no need for waiting in a long queue. Accordingly, over 10 percent of all HPC jobs are running in clouds, and over 70 percent of HPC centers run some jobs in a cloud as of June 2019; the latter is up from just 13 percent in 2011 (Hyperion Research, 2019).

In short, cloud computing is now a cost-effective option for statisticians who are in demand for high performance, with not so a steep learning curve.

2.3. Multi-GPU node

In some cases, HPC is achieved by installing multiple GPUs on a single node. Over the past two decades, GPUs have gained a sizable amount of popularity among scientists. GPUs were originally designed to aid CPUs in rendering graphics for video games quickly. A key feature of GPUs is their ability to apply a mapping to a large array of floating-point numbers simultaneously. The mapping (called a *kernel*) can be programmed by the user. This feature is enabled by integrating a massive number of simple compute cores in a single processor chip, realizing the SIMD architecture. While this architecture of GPUs was created in need of generating a large number of pixels in a limited time due to the frame rate constraint of high-quality video games, the programmability and high throughput soon gained attention from the scientific computing community. Matrix-vector multiplication and elementwise

nonlinear transformation of a vector can be computed several orders of magnitudes faster on GPU than on CPU. Early applications of general-purpose GPU programming include physics simulations, signal processing, and geometric computing (Owens et al., 2007). Technologically savvy statisticians demonstrated its potential in Bayesian simulation (Suchard, Holmes and West, 2010; Suchard, Wang, Chan, Frelinger, Cron and West, 2010) and high-dimensional optimization (Zhou et al., 2010; Yu et al., 2015). Over time, the number of cores has increased from 240 (Nvidia GTX 285, early 2009) to 4608 (Nvidia Titan RTX, late 2018) and more local memory — separated from CPU’s main memory — has been added (from 1GB of GTX 285 to 24GB for Titan RTX). GPUs could only use single-precision for their floating-point operations, but they now support double- and half-precisions. More sophisticated operations such as tensor operations are also supported. High-end GPUs are now being designed specifically for scientific computing purposes, sometimes with fault-tolerance features such as error correction.

A major drawback of GPUs for statistical computing is that GPUs have a smaller memory compared to CPU, and it is slow to transfer data between them. Using multiple GPUs can be a cure: recent GPUs can be installed on a single node and communicate with each other without the meddling of CPU; this effectively increases the local memory of a collection of GPUs. (Lee et al. (2017) explored this possibility in image-based regression.) It is relatively inexpensive to construct a node with 4–8 desktop GPUs compared to a cluster of CPU nodes with a similar computing power (if the main computing tasks are well suited for the SIMD model), and the gain is much larger for the cost. Linear algebra operations that frequently occur in high-dimensional optimization is a good example.

Programming environments for GPU computing have been notoriously hostile to programmers for a long time. The major sophistication is that a programmer needs to write two suits of code, the *host* code that runs on a CPU and *kernel* functions that run on GPU(s). Data transfer between CPU and GPU(s) also has to be taken care of. Moreover, kernel functions need to be written in special extensions of C, C++, or Fortran, e.g., CUDA (Nvidia, 2007) or OpenCL (Munshi, 2009). Combinations of these technical barriers made casual programmers, e.g., statisticians, to keep away from writing GPU code despite its computational gains. There were efforts to sugar-coat these hostile environments with a high-level language such as R (Buckner et al., 2009) or Python (Tieleman, 2010; Klöckner et al., 2012; Lam et al., 2015), but these attempts struggled to garner big enough user base to maintain the community in general. The functionalities were often limited and inherently hard to extend.

Fortunately, GPU programming environments have been revolutionized since deep learning (LeCun et al., 2015) brought sensation in many machine learning applications. Deep learning is almost synonymous to deep neural networks, which refer to a repeated (“layered”) application of an affine transformation of the input followed by identical elementwise transformations through a nonlinear link function, or “activation function.” Fitting a deep learning model is almost always conducted via (approximate) minimization of the specified loss function through a clever application of the chain rule to the gradient descent method, called “backpropagation” (Rumelhart et al., 1988). These computational features fit well to the SIMD architecture of GPUs, use of which dramatically reduces the training time of this highly overparameterized family of models with a huge amount of training data (Raina et al., 2009). Consequently, many efforts had been made to ease GPU programming for deep learning, resulting in easy-to-use software libraries. Since the sizes of neural networks get ever larger, more HPC capabilities, e.g., support for multiple GPUs and CPU clusters, have been developed. As we review in the next section, programming with those libraries gets rid of many hassles with GPUs, close to the level of conventional programming.

Readers might ask: why should statisticians care about deep learning software? As Cheng

and Titterton (1994) pointed out 25 years ago, “neural networks provide a representational framework for familiar statistical constructs,” and “statistical techniques are sometimes implementable using neural-network technology.” For example, linear regression is just a simple neural network with a single layer and linear activation functions. Many more sophisticated statistical frameworks can be mapped to that of neural networks and can benefit from those ease-to-use deep learning libraries for computational performance boosting.

3. Easy-to-use Software Libraries for HPC

3.1. Deep learning libraries and HPC

As of writing this article (late 2019), the two most popular deep learning software libraries are TensorFlow (Abadi et al., 2016) and PyTorch (Paszke et al., 2017). There are two common features of these libraries. One is the computation graph that automates the evaluation of the loss function and its differentiation required for backpropagation. The other feature, more relevant to statistical computing, is an efficient and user-friendly interface to linear algebra and convolution routines that work on both CPU and GPU in a unified fashion. A typical pattern of using these libraries is to specify the model and describe how to fit the model to the training data in a high-level scripting language (mostly Python). To fit a model, the software selects a backend optimized for the system in which the model runs. If the target system is a CPU node, then the software can be configured to utilize the OpenBLAS (Xianyi et al., 2014) or the Intel Math Kernel Library (Wang et al., 2014), which are optimized implementations of the Basic Linear Algebra Library (BLAS, Blackford et al., 2002) for shared-memory systems. If the target system is a workstation with a GPU, then the same script can employ a pair of host and kernel code that may make use of cuBLAS (NVIDIA, 2013), a GPU version of BLAS, and cuSPARSE (NVIDIA, 2018), GPU-oriented sparse linear algebra routines. Whether to run the model on a CPU or GPU can be controlled by a slight change in the option for device selection, which is usually a line or two of the script. From the last paragraph of the previous section, we see that this “write once, run everywhere” feature of deep learning libraries can make GPU programming easier for statistical computing as well.

TensorFlow is a successor of Theano (Bergstra et al., 2011), one of the first libraries to support symbolic differentiation based on computational graphs. Unlike Theano that generates GPU code on the fly, TensorFlow is equipped with pre-compiled GPU code for a large class of pre-defined operations. The computational graph of TensorFlow is static so that a user has to pre-define all the operations prior to execution. Unfortunately, such a design does not go along well with the philosophy of scripting languages that the library should work with and makes debugging difficult. To cope with this issue, an “eager execution” mode, which executes commands without building a computational graph, is supported.

PyTorch inherits Torch (Collobert et al., 2011), an early machine learning library written in a functional programming language called Lua, and Caffe (Jia et al., 2014), a Python-based deep learning library. Unlike TensorFlow, PyTorch uses dynamic computation graphs, so it does not require computational graphs to be pre-defined. Thanks to this dynamic execution model, the library is more intuitive and flexible to the user than most of its competitors. PyTorch (and Torch) can also manage GPU memory efficiently. As a result, it is known to be faster than other deep learning libraries (Bahrampour et al., 2015).

Both libraries support multi-GPU and multi-node computing. In Tensorflow, multi-GPU computation is supported natively. If data are distributed in multiple GPUs and one needs data from the other, the GPUs communicate implicitly and the user does not need to care. Multi-node communication is more subtle: while remote procedure call is supported natively

in the same manner as multi-GPU communications, it is recommended to use MPI through the library called Horovod (Sergeev and Del Balso, 2018) for tightly-coupled HPC environments (more information is given in Section 3.2). In PyTorch, both multi-GPU and multi-node computing are enabled by using the interface `torch.distributed`. This interface defines MPI-style (but simplified) communication primitives (see the *parallel programming models* paragraph in Section 2.1), whose specific implementation is called a backend. Possible communication backends include the MPI, Nvidia Collective Communications Library (NCCL), and Gloo (Solo.io, n.d.). NCCL is useful for a multi-GPU node; (CUDA-aware) MPI maps multi-GPU communications to the MPI standard as well as traditional multi-node communications; Gloo is useful in cloud environments.

This feature of unified interfaces for various HPC environments is supported through operator overloading or polymorphism in modern programming languages, but achieving this seamlessly with a single library, along with multi-device support, is remarkable. This is partially because of injection of capital in pursuit of commercial promises of deep learning (TensorFlow is being developed by Google, and PyTorch by Facebook). There are other deep learning software libraries with similar HPC supports: Apache MxNet (Chen et al., 2015) supports multi-node computation via Horovod; multi-GPU computing is also supported at the interface level. Microsoft Cognitive Toolkit (CNTK, Seide and Agarwal, 2016) supports parallel stochastic gradient algorithms through MPI.

3.2. Case study: PyTorch versus TensorFlow

In this section, we illustrate how simple it is to write a statistical computing code on multi-device HPC environments using a modern deep learning libraries. We compare PyTorch and TensorFlow code written in Python, which computes a Monte Carlo estimate of the constant π . The emphasis is on readability and flexibility, i.e., how small a modification is needed to run the code written for a single-CPU node on a multi-GPU node and a multi-node system.

Listing 1 shows the Monte Carlo π estimation code for PyTorch. Even for those who are not familiar with Python, the code should be quite readable. The main workhorse is function `mc_pi()` (Lines 14–21), which generates a sample of size n from the uniform distribution on $[0, 1]^2$ and compute the proportion of the points that fall inside the quarter circle of unit radius centered at the origin. Listing 1 is a fully executable program. It uses `torch.distributed` interface with an MPI backend (Line 3). An instance of the program of Listing 1 is attached to a device and is executed as a “process”. Each process is given its identifier (rank), which is retrieved in Line 5. The total number of processes is known to each process via Line 6. After the proportion of the points in the quarter-circle is computed in Line 17, each process gathers the sum of the means computed from all the processes in Line 18 (this is called the all-reduce operation; see Section 2.1). Line 19 divides the sum by the number of processes, yielding a Monte Carlo estimate of π based on the sample size of $n \times (\text{number of processes})$.

We have been deliberately ambiguous about the “devices.” Here, a CPU core or a GPU is referred to as a device. Listing 1 assumes the environment is a workstation with one or more GPUs, and the backend MPI is CUDA-aware. A CUDA-aware MPI, e.g., OpenMPI (Gabriel et al., 2004), allows data to be sent directly from a GPU to another GPU through the MPI protocols. Lines 9–10 specify that the devices to use in the program are GPUs. If the environment is a cluster with multiple CPU nodes (or even a single node), then all we need to do is changing Line 9 to `device = 'cpu'`. The resulting code runs on a cluster seamlessly.

In TensorFlow, however, a separate treatment to multi-GPU and cluster settings is almost necessary. The code for multi-GPU setting is similar to Listing 1 hence given in Appendix

```
1 import torch.distributed as dist
2 import torch
3 dist.init_process_group('mpi') # initialize MPI
4
5 rank = dist.get_rank()        # device id
6 size = dist.get_world_size()  # total number of devices
7
8 # select device
9 device = 'cuda:{}'.format(rank) # or simply 'cpu' for CPU computing
10 if device.startswith('cuda'): torch.cuda.set_device(rank)
11
12 def mc_pi(n):
13     # this code is executed on each device.
14     x = torch.rand((n), dtype=torch.float64, device=device)
15     y = torch.rand((n), dtype=torch.float64, device=device)
16     # compute local estimate of pi
17     r = torch.mean((x**2 + y**2 < 1).to(dtype=torch.float64))*4
18     dist.all_reduce(r) # sum of 'r's in each device is stored in 'r'
19     return r / size
20
21 if __name__ == '__main__':
22     n = 10000
23     r = mc_pi(n)
24     if rank == 0:
25         print(r.item())
```

Listing 1: Distributed Monte Carlo estimation of π for PyTorch

B. In a cluster setting, unfortunately, it is extremely difficult to reuse the multi-GPU code. If direct access to individual compute nodes is available, that information can be used to run the code distributedly, albeit not being much intuitive. However, in HPC environments where computing jobs are managed by job schedulers, we often do not have direct access to the compute nodes. The National Energy Research Scientific Computing Center (NERSC), the home of the 13th most powerful supercomputers in the world (as of November 2019), advises that gRPC, the default inter-node communication method of TensorFlow, is very slow on tightly-coupled nodes, thus recommends a direct use of MPI (NERSC, n.d.). Using MPI with TensorFlow requires an external library called Horovod and a substantial modification of the code, as shown in Listing 2. This is a sharp contrast to Listing 1, where essentially the same PyTorch code can be used in both multi-GPU and multi-node settings.

Therefore we employ PyTorch in the sequel to implement the highly parallelizable algorithms of Section 4 in a multi-GPU node and a cluster on a cloud, as it allows simpler code that runs on various HPC environments with a minimal modification. (In fact this modification can be made automatic through a command line argument.)

4. Highly Parallelizable Algorithms

In this section, we discuss some easily parallelizable optimization algorithms useful for fitting high-dimensional statistical models, assuming that data are so large that they have to be stored distributedly. These algorithms can benefit from the distributed-memory environment by using relatively straightforward operations, via distributed matrix-vector multiplication and independent update of variables.

```
1 import tensorflow as tf
2 import horovod.tensorflow as hvd
3
4 # initialize horovod
5 hvd.init()
6 rank = hvd.rank()
7
8 # without this block, all the processes try to allocate
9 # all the memory from each device, causing out of memory error.
10 devices = tf.config.experimental.list_physical_devices("GPU")
11 if len(devices) > 0:
12     for d in devices:
13         tf.config.experimental.set_memory_growth(d, True)
14
15 # select device
16 tf.device("device:gpu:{}".format(rank)) # tf.device("device:cpu:0") for CPU
17
18 # function runs in parallel with (graph computation/lazy-evaluation)
19 # or without (eager execution) the line below
20 @tf.function
21 def mc_pi(n):
22     # this code is executed on each device
23     x = tf.random.uniform((n,), dtype=tf.float64)
24     y = tf.random.uniform((n,), dtype=tf.float64)
25     # compute local estimate for pi and save it as 'estim'.
26     estim = tf.reduce_mean(tf.cast(x**2 + y ** 2 <1, tf.float64))*4
27     # compute the mean of 'estim' over all the devices
28     estim = hvd.allreduce(estim)
29     return estim
30
31 if __name__ == '__main__':
32     n = 10000
33     estim = mc_pi(n)
34     # print the result on rank zero
35     if rank == 0:
36         print(estim.numpy())
```

Listing 2: Monte Carlo estimation of π for TensorFlow on multiple nodes using Horovod

4.1. MM algorithms

The MM principle (Lange et al., 2000; Lange, 2016), where “MM” stands for either majorization-minimization or minorization-maximization, is a useful tool for constructing parallelizable optimization algorithms. In minimizing an objective function $f(x)$ iteratively, for each iterate we consider a surrogate function $g(x|x^n)$ satisfying two conditions: the tangency condition $f(x^n) = g(x^n|x^n)$ and the domination condition $f(x) \leq g(x|x^n)$ for all x . Updating $x^{n+1} = \arg \min_x g(x|x^n)$ guarantees that $\{f(x^n)\}$ is a nonincreasing sequence:

$$f(x^{n+1}) \leq g(x^{n+1}|x^n) \leq g(x^n|x^n) = f(x^n).$$

In fact, full minimization of $g(x|x^n)$ is not necessary for the descent property to hold; merely decreasing it is sufficient. The EM algorithm (Dempster et al., 1977) is an instance of the MM principle. In order to maximize the marginal loglikelihood

$$\ell(\theta) = \log \int p_\theta(o, z) dz,$$

where o is the observed data, z is unobserved missing data, and θ is the parameter to estimate, we maximize the surrogate function

$$Q(\theta|\theta^n) = \mathbb{E}_{Z|X, \theta^n} [\log p_\theta(o, z)] = \int \log [p_\theta(o, z)] p_{\theta^n}(z|o) dz,$$

since

$$\begin{aligned} \ell(\theta) &= \log \int p_\theta(o, z) dz = \log \int \frac{p_\theta(o) p_\theta(z|o)}{p_{\theta^n}(z|o)} p_{\theta^n}(z|o) dz \\ &\geq \int \log \left[\frac{p_\theta(o) p_\theta(z|o)}{p_{\theta^n}(z|o)} \right] p_{\theta^n}(z|o) dz \\ &= Q(\theta|\theta^n) - \int \log [p_{\theta^n}(z|o)] p_{\theta^n}(z|o) dz \end{aligned}$$

by Jensen’s inequality, and the second term in the last inequality is irrelevant to θ . (See Wu and Lange (2010) for more details about the relation between MM and EM.)

MM updates are usually designed to make a nondifferentiable objective function smooth, linearize the problem, or avoid matrix inversions by a proper choice of the surrogate function. MM is naturally well-suited for parallel computing environments, as we can choose a separable surrogate function and update variables independently. For example, when maximizing loglikelihoods, a term involving summation inside the logarithm $\log(\sum_{i=1}^p u_i)$ often arises. By Jensen’s inequality, this term can be minorized and separated as

$$\log\left(\sum_{i=1}^p u_i\right) \geq \sum_{i=1}^p \frac{u_i^n}{\sum_{j=1}^p u_j^n} \log\left(\frac{\sum_{j=1}^p u_j^n}{u_i^n} u_i\right) = \sum_{i=1}^p \frac{u_i^n}{\sum_{j=1}^p u_j^n} \log u_i + c_n,$$

where u_i^n ’s are constants and c_n is a constant only depending on u_i^n ’s. Parallelization of MM algorithms on a single GPU using separable surrogate functions is extensively discussed in Zhou et al. (2010). Separable surrogate functions are especially important in distributed environments, e.g. multi-GPU systems.

4.2. Proximal gradient descent

The proximal gradient descent method is an extension of the gradient descent method, which deals with minimization of sum of two convex functions, i.e.,

$$\min_x f(x) + g(x).$$

Function f is possibly nondifferentiable, while g is continuously differentiable.

We first define the proximity operator of f :

$$\mathbf{prox}_{\lambda f}(y) = \arg \min_x \left\{ f(x) + \frac{1}{2\lambda} \|x - y\|_2^2 \right\}, \quad \lambda > 0$$

For many functions their proximity operators take closed forms. We say such functions “proximable”. For example, consider the $0/\infty$ indicator function of a closed convex set C

$$\delta_C(x) = \begin{cases} 0, & x \in C \\ +\infty, & x \notin C \end{cases}.$$

The corresponding proximity operator is the Euclidean projection onto C : $P_C(y) = \arg \min_{x \in C} \|y - x\|_2$. The proximity operator of the ℓ_1 -norm $\lambda \|\cdot\|_1$ is the soft-thresholding operator:

$$[\mathcal{S}_\lambda(y)]_i := \text{sign}(y_i)(|y_i| - \lambda)_+$$

For many sets, e.g., nonnegative orthant, P_C is simple to compute.

Now we proceed with the proximal gradient descent for minimization of $h(x) = f(x) + g(x)$. Assume g is convex and has L -Lipschitz gradients, i.e., $\|g(x) - g(y)\|_2 \leq L\|x - y\|_2$ for all x, y in the interior of its domain, and f is lower-semicontinuous, convex, and proximable. The L -Lipschitz gradients naturally result in following surrogate function that majorizes h :

$$\begin{aligned} h(x) &\leq f(x) + g(x^n) + \langle \nabla g(x^n), x - x^n \rangle + \frac{L}{2} \|x - x^n\|_2^2 \\ &= f(x) + g(x^n) + \frac{L}{2} \left\| x - x^n + \frac{1}{L} \nabla g(x^n) \right\|_2^2 - \frac{1}{2L} \|\nabla g(x^n)\|_2^2 =: p(x|x^n). \end{aligned}$$

Minimizing $p(x|x^n)$ with respect to x results in the update:

$$x^{n+1} = \mathbf{prox}_{\gamma_n f}(x^n - \gamma_n \nabla g(x^n)), \quad \gamma_n \in \left(0, \frac{1}{L}\right]. \quad (1)$$

This update guarantees a nonincreasing sequence of $h(x^n)$ by the MM principle. Proximal gradient method also has an interpretation of forward-backward operator splitting, and the step size $\gamma_n \in (0, \frac{2}{L})$ guarantees convergence (Combettes and Pesquet, 2011; Bauschke and Combettes, 2011; Combettes, 2018). If $f(x) = \delta_C(x)$, then the corresponding algorithm is called the projected gradient method. If $f(x) = \lambda \|x\|_1$, then the corresponding algorithm is the iterative shrinkage-thresholding algorithm (ISTA, Beck and Teboulle, 2009). For many functions f , the update (1) is simple and easily parallelized, thus the algorithm is suitable for HPC computing. For example, the soft-thresholding operator is elementwise hence the updates are independent. In addition, if $f(x) = -a \log x$, then

$$\mathbf{prox}_{\gamma f}(y) = \frac{y + \sqrt{y^2 + 4\gamma a}}{2}. \quad (2)$$

This proximity operator is useful for the example in Section 6.2. See Parikh and Boyd (2014) for a thorough review and distributed-memory implementations, and Polson et al. (2015) for a statistics-oriented review.

4.3. Primal-dual methods

The algorithms discussed so far are primal methods. Primal-dual methods introduce additional dual variables but can deal with a larger class of problems. Consider the problems of the form $h(x) = f(Kx) + g(x)$, where K is a linear map. We further assume that f , g are lower semicontinuous, convex, and proper functions. Even if f is proximable, the proximity operator for $f(K\cdot)$ is not easy to compute. Define the convex conjugate of f as $f^*(y) = \sup_x \langle x, y \rangle - f(x)$. It is known that $f^{**} = f$ since f is lower semicontinuous and convex, so $f(Kx) = f^{**}(Kx) = \sup_y \langle Kx, y \rangle - f^*(y)$. Then the minimization problem $\inf_x f(Kx) + g(x)$ is equivalent to the saddle-point problem

$$\inf_x \sup_y \langle Kx, y \rangle + g(x) - f^*(y).$$

Under mild conditions strong duality

$$\inf_x \sup_y \langle Kx, y \rangle + g(x) - f^*(y) = \sup_y \inf_x \langle x, K^T y \rangle + g(x) - f^*(y)$$

holds and the saddle point (\hat{x}, \hat{y}) satisfies the optimality conditions

$$K\hat{x} - \partial f^*(\hat{y}) \ni 0 \text{ and } K^T \hat{y} + \partial g(\hat{x}) \ni 0,$$

where $\partial\phi$ denotes the subdifferential of a convex function ϕ . The vector y is the dual variable and the maxmin problem

$$\sup_y \inf_x \langle x, K^T y \rangle + g(x) - f^*(y) = \sup_y -f^*(y) - g^*(-K^T y)$$

is called the dual of the original (primal) minimization problem.

A widely known method to solve this saddle point problem in the statistical literature is the ADMM (Xue et al., 2012; Zhu, 2017; Ramdas and Tibshirani, 2016; Gu et al., 2018). The ADMM update is given by:

$$x^{n+1} = \arg \min_x f(x) + (t/2) \|Kx - \tilde{x}^n + (1/t)y^n\|_2^2 \quad (3a)$$

$$\tilde{x}^{n+1} = \mathbf{prox}_{(1/t)h}(Kx^{n+1} + (1/t)y^n) \quad (3b)$$

$$y^{n+1} = y^n + t(Kx^{n+1} - \tilde{x}^{n+1}). \quad (3c)$$

The update (3a) is *not* a proximity operator, as the quadratic term is not spherical. It defines an inner optimization problem that is often nontrivial. In the simplest case of f being linear or quadratic (which arises in linear regression), (3a) involves solving a linear system. While it is plausible to obtain the inverse of the involved matrix once and reuse it for future iterations, inverting a matrix even once quickly becomes intractable in the high-dimensional setting, as its time complexity is cubic in the number of variables.

The primal-dual hybrid gradient method (PDHG, Zhu and Chan, 2008; Esser et al., 2010; Chambolle and Pock, 2011) avoids such inversion via the following iteration:

$$y^{n+1} = \mathbf{prox}_{\sigma f^*}(y^n + \sigma K \bar{x}^n) \quad (4a)$$

$$x^{n+1} = \mathbf{prox}_{\tau g}(x^n - \tau K^T y^{n+1}) \quad (4b)$$

$$\bar{x}^{n+1} = 2x^{n+1} - x^n, \quad (4c)$$

where (4a) and (4b) are dual ascent and primal descent steps, respectively; σ and τ are step sizes. The last step (4c) corresponds to the extrapolation. If f is proximable, so is f^* ,

since $\mathbf{prox}_{\gamma f^*}(x) = x - \gamma \mathbf{prox}_{\gamma^{-1}f}(\gamma^{-1}x)$ by Moreau’s decomposition. This method has been studied using monotone operator theory (Condat, 2013; Vü, 2013; Ko et al., 2019+). Convergence of iteration (4) is guaranteed if $\sigma\tau\|K\|_2^2 < 1$, where $\|M\|_2$ is the spectral norm of matrix M . If g has L -Lipschitz gradients, then the proximal step (4b) can be replaced by a gradient step

$$x^{n+1} = x^n - \tau(\nabla g(x^n) + K^T y^{n+1}).$$

The PDHG algorithms are also highly parallelizable as long as the involved proximity operators are easy to compute and separable; no matrix inversion is involved in iteration (4) and only matrix-vector multiplications appear.

5. Distributed matrix data structure for PyTorch

For the forthcoming examples and potential future uses in statistical computing, we propose a simple distributed matrix data structure named `distmat`. In this structure, each process, enumerated by its rank, holds a contiguous block of the full data matrix by rows or columns. The data may be a sparse matrix. If GPUs are involved, each process controls a GPU whose index matches the process rank. For notational simplicity, we denote the dimension to split in square brackets. If a $[100] \times 100$ matrix is split over four processes, the process with rank 0 keeps the first 25 rows of the matrix, and the rank 3 process takes the last 25 rows. For the sake of simplicity, we always assume that the size along the split dimension is divided by the number of processes. The code along with the examples in Section 6 is available at http://stat.snu.ac.kr/compstat/software/dist_stat.html.

In `distmat`, unary elementwise operations such as exponentiation, square root, absolute value, and logarithm of matrix entries were implemented in an obvious way. Binary elementwise operations such as addition, subtraction, multiplication, division were implemented in a similar manner to R’s vector recycling. For example, if two matrices of different dimensions are to be added together, say one is three-by-four and the other is three-by-one, the latter matrix is expanded to a three-by-four matrix with the column repeated four times. Another example is adding a one-by-three matrix and a four-by-one matrix. The former matrix is expanded to a four-by-three matrix by repeating the row four times, and the latter to a four-by-three matrix by repeating the column three times. Application of this concept is natural using the broadcast semantics of PyTorch. Reduction operations, such as row-wise (column-wise, and matrix-wise) summation, (maximum, and minimum) were also implemented in a similar fashion.

Matrix multiplications are more subtle. Six different scenarios of matrix-matrix multiplications, each representing a different configuration of the split dimension of two input matrices and the output matrix, were considered and implemented. These scenarios are listed in Table 1. Note that “broadcasting” and “reduction” in this paragraph are defined over a matrix dimension (rows or columns), unlike in the other parts of this article where they are defined over multiple processes or ranks. The implementation of each case is carried out using the collective communication directives introduced in Section 2.1. Matrix multiplication scenarios are automatically selected based on the shapes of the input matrices A and B , except for the Scenarios 1 and 3 sharing the same input structure. Those two are further distinguished by the shape of output, AB . The nonnegative matrix factorization example of Section 6.1, which utilizes `distmat` most heavily among others, involves Scenarios 1 to 5. Scenario 6 is for matrix-vector multiplications, where broadcasting small vectors is almost always efficient.

In Listing 3, we demonstrate an example usage of `distmat`. We assume that this program is run with 4 processes (`size` in Line 5 is 4). Line 11 generates a $[4] \times 4$ double-precision

Table 1: Six distributed matrix multiplication configurations. Matrix with no distributed dimension is duplicated in all the processes. Sizes p and q are assumed to be much larger than r and s .

	A	B	AB	Description	Usage in Section 6
1	$r \times [p]$	$[p] \times q$	$r \times [q]$	Inner product, result distributed.	$V^T X$
2	$[p] \times q$	$[q] \times r$	$[p] \times r$	Fat matrix multiplied by a thin and tall matrix.	XW^T
3	$r \times [p]$	$[p] \times s$	$r \times s$	Inner product, result broadcasted. Suited for inner product between two thin matrices.	$V^T V, WW^T$
4	$[p] \times r$	$r \times [q]$	$[p] \times q$	Outer product, may require large amount of memory. Often used to compute objective function.	VW
5	$[p] \times r$	$r \times s$	$[p] \times s$	A distributed matrix multiplied by a small, broadcasted matrix.	VC where $C = WW^T$; CW where $C = V^T V$
6	$r \times [p]$	$p \times s$	$r \times s$	A distributed matrix multiplied by a thin and tall broadcasted matrix. Intended for matrix-vector multiplications.	Ax

matrix on CPU sampled from the uniform distribution. The function `distgen_uniform` has an optional argument `TType` that allows users to choose the data type and location of the matrix: Line 10 specifies the matrix to be a double-precision matrix on CPU. The user may change it to `torch.cuda.FloatTensor` to create this matrix on a GPU with single-precision. Line 13 multiplies the two matrices `A` and `B` to form a distributed matrix of size $[4] \times 2$. The matrix multiplication routine internally chooses to utilize Scenario 2 in Table 1. In order to compute $\log(1 + AB)$ elementwise, all that is needed to do is to write $(1 + AB).log()$ as in Line 17. Here, $1 + AB$ is computed elementwise first, then its logarithms are computed. The local block of data can be accessed by appending `.chunk` to the name of the distributed matrix, as in Lines 16 and 20.

```

1 import torch, distmat
2 import torch.distributed as dist
3 dist.init_process_group('mpi')
4 rank = dist.get_rank()
5 size = dist.get_world_size()
6
7 device = 'cuda:{}'.format(rank) # or simply 'cpu' for CPU computing
8 if device.startswith('cuda'): torch.cuda.set_device(rank)
9
10 tensortype = torch.DoubleTensor # torch.cuda.FloatTensor for a single-precision
    matrix on a GPU
11 A = distmat.distgen_uniform(4, 4, TType=tensortype)
12 B = distmat.distgen_uniform(4, 2, TType=tensortype)
13 AB = distmat.mm(A, B) # A * B
14 if rank == 0: # to print this only once
15     print("AB = ")
16 print(rank, AB.chunk) # print the rank's portion of AB.
17 C = (1 + AB).log() # elementwise logarithm
18 if rank == 0:
19     print("log(1 + AB) = ")
20 print(rank, C.chunk) # print the rank's portion of C.

```

Listing 3: An example usage of the module `distmat`.

6. Examples

In this section, we compare the performance of the optimization algorithms on four statistical computing examples: nonnegative matrix factorization (NMF), positron emission tomography (PET), multidimensional scaling (MDS), and ℓ_1 -regularized Cox model for survival analysis. We demonstrate single-device codes to show the simplicity of the programming and distribute it over a cluster consisted of multiple AWS EC2 instances or a local multi-GPU workstation. For NMF and PET, we compare two algorithms, one more classical, and the other based on recent development. We evaluate the objective function once per 100 iterations. For the comparison of execution time, the iteration is run for a fixed number of iterations, regardless of convergence. For comparison of different algorithms regarding the same problem, we iterate until $\frac{|f(\theta^n) - f(\theta^{n-100})|}{100(|f(\theta^n)| + 1)} < 10^{-7}$. Table 2 shows the setting of our HPC systems used for the experiments. For virtual cluster experiments, we utilized 1 to 20 of AWS `c5.18xlarge` instances with 36 physical cores with AVX-512 (512-bit advanced vector extension to the x86 instruction set) enabled in each instance through `CfnCluster`. Network bandwidth of each `c5.18xlarge` instance was 25GB/s. A separate `c5.18xlarge`

TABLE 2
Configuration of experiments

	local node		AWS c5.18xlarge
	CPU	GPU	CPU
Model	Intel Xeon E5-2680 v2	Nvidia GTX 1080	Intel Xeon Platinum 8124M
# of cores	10	2560	18
Clock	2.8 GHz	1.6 GHz	3.0GHz
# of entities	2	8	2 (per instance) × 1-20 (instances)
Total memory	256 GB	64 GB	144 GB × 1-20
Total cores	20	20,480 (CUDA)	36 × 1-20

instance served as the “master” instance. This instance does not participate in computation by itself but manages the computing jobs over the 1 to 20 “worker” instances. Data and software for the experiments were stored in an Amazon Elastic Block Store (EBS) volume attached to this instance and shared among the worker instances via the network file system. Further details are given in Appendix C. For GPU experiments, we used a local machine with two CPUs (10 cores per CPU) and eight Nvidia GTX 1080 GPUs. These are desktop GPUs, not optimized for double-precision. All the experiments were conducted using PyTorch version 0.4 built on the MKL; the released code works for the versions up to 1.3, the most recent stable version as of December 2019.

For all of our experiments, the single-precision computation results on GPU were almost the same as the double-precision result up to six significant digits, except for ℓ_1 -regularized Cox regression, the necessary cumulative sum operation implemented in PyTorch caused numerical instability in some cases with small penalties. Therefore all the computations for Cox regression were performed in double-precision. Extra efforts for writing a multi-device code were modest using `distmat`. Given around 1000 lines of code to implement basic operations for multi-device configuration in `distmat`, additional code for our four applications was less than 30 lines for each application.

As can be verified in the sequel, computing on GPUs was effective on mid-sized (around $10,000 \times 10,000$) datasets, but stalled on larger (around $100,000 \times 100,000$) datasets due to memory limitation. In contrast, the virtual clusters were not very effective on mid-sized data, and may even slow down due to communication burden. They were effective and scaled well on larger (around $100,000 \times 100,000$) datasets.

6.1. Nonnegative matrix factorization

NMF is a procedure that approximates a nonnegative data matrix $X \in \mathbb{R}^{m \times p}$ by a product of two low-rank nonnegative matrices, $V \in \mathbb{R}^{m \times r}$ and $W \in \mathbb{R}^{r \times p}$. It is widely used in image processing, bioinformatics, and recommender systems (Wang and Zhang, 2013) where the data have only nonnegative values. One of the first effective algorithms was the multiplicative algorithm introduced by Lee and Seung (1999, 2001). In a simple setting, NMF minimizes

$$f(V, W) = \|X - VW\|_{\mathbb{F}}^2,$$

where $\|\cdot\|_{\mathbb{F}}$ denotes the Frobenius norm.

The multiplicative algorithm written using PyTorch for a single device is given in Listing 4. This algorithm can be interpreted as a case of MM algorithm with a surrogate function of f based on Jensen’s inequality:

$$g(V, W|V^n, W^n) = \sum_{i,j,k} \frac{v_{ik}^n w_{kj}^n}{\sum_{k'} v_{ik'}^n w_{k'j}^n} \left(x_{ij} - \frac{\sum_{k'} v_{ik'}^n w_{k'j}^n}{v_{ik}^n w_{kj}^n} v_{ik} w_{kj} \right)^2.$$

The update rule is:

$$\begin{aligned} V^{n+1} &= V^n \odot [X(W^n)^T] \oslash [V^n W^n (W^n)^T] \\ W^{n+1} &= W^n \odot [(V^{n+1})^T X] \oslash [(V^{n+1})^T V^{n+1} W^n], \end{aligned}$$

where \odot and \oslash denote elementwise multiplication and division, respectively.

```

1 # initialize X, W, V in a single device: a CPU or a GPU.
2 for i in range(max_iter):
3     # Update V
4     XWt = torch.mm(X, W.t()) # compute XW^T
5     WWt = torch.mm(W, W.t()) # compute WW^T
6     VWWt = torch.mm(V, WWt) # compute VWW^T
7     # V = V * XW^T / VWW^T elementwise. In-place operation.
8     V = V.mul_(XWt).div_(VWWt)
9     # Update W
10    VtX = torch.mm(V.t(), X)
11    VtV = torch.mm(V.t(), V)
12    VtVW = torch.mm(VtV, W)
13    W = W.mul_(VtX).div_(VtVW)

```

Listing 4: A PyTorch code for multiplicative NMF update on a single shared-memory systems.

The simple-looking code in Listing 4 can fully utilize the shared-memory parallelism: if the matrices are stored on the CPU memory, it runs parallelly, fully utilizing OpenMP and MKL/OpenBLAS (depending on installation). If they are stored on a single GPU, it runs parallelly utilizing GPU cores through the CUDA libraries. Distributing this algorithm on a large scale machine is straightforward (Liu et al., 2010).

Figure 1 shows an example of NMF on a publicly available hyperspectral image. It was acquired by the reflective optics system imaging spectrometer sensor in a flight campaign over Pavia University in Italy. The image is essentially a 610 (height) \times 340 (width) \times 103 (bands) hyperspectral cube. It is interpreted as a 207,400 (pixels) \times 103 (bands) matrix and then analyzed using NMF. The rank r was set to 20. In the resulting 207,400 \times 20 matrix V , each column can be interpreted as a composite channel from the original 103 bands. Three of these channels showing distinct features chosen by hand are shown in Figure 1.

A problem with the multiplicative algorithm is the potential to generate subnormal numbers, significantly slowing down the algorithm. A subnormal number or denormal number is a number smaller (in magnitude) than the smallest positive number that can be represented by the floating-point number system. Subnormal numbers are generated by the multiplicative algorithm if values smaller than 1 are multiplied repeatedly. Indeed, when Listing 4 was run on a CPU with a small synthetic data of size 100 \times 100, we observed a significant slowdown. The IEEE floating-point standard is to deal with subnormal numbers properly with a special hardware or software implementation (IEEE Standards Committee, 2008). In many CPUs, the treatment of subnormal numbers relies on software and hence is very slow. Forcing such value to zero is potentially dangerous depending on applications because it becomes prone to division-by-zero error. In our experiments, we did not observe division-by-zero error when flushing the subnormal numbers to zero. In contrast, Nvidia GPUs support

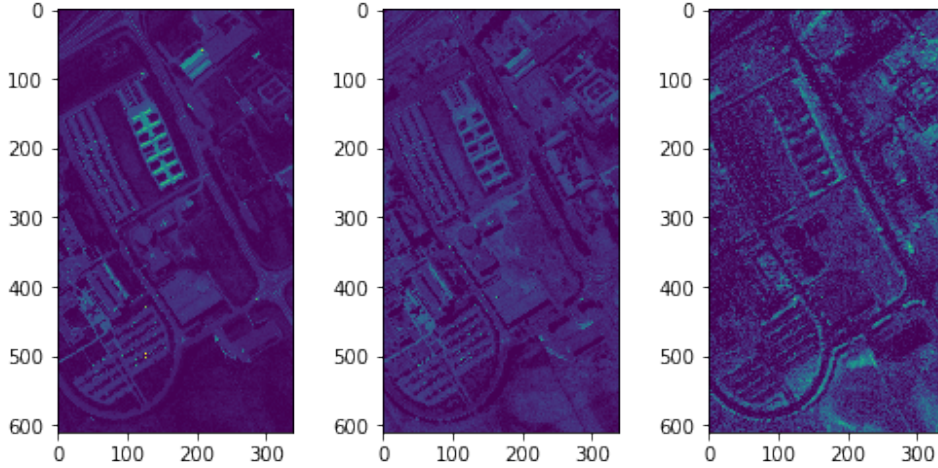


Fig 1: Three selected bands from the NMF of the Pavia University hyperspectral image with $r = 20$

subnormal numbers at a hardware level since the Fermi architecture, and simple arithmetic operations do not slow down by subnormal numbers (Whitehead and Fit-Florea, 2011).

Subnormal numbers can be completely avoided (especially in CPUs) by using a different algorithm. The alternating projected gradient (APG) method (Lin, 2007) is such an algorithm, and it is also easy to introduce regularization terms. With ridge penalties the objective function

$$f(V, W; \epsilon) = \|X - VW\|_F^2 + \frac{\epsilon}{2}\|V\|_F^2 + \frac{\epsilon}{2}\|W\|_F^2$$

is minimized. The corresponding APG update is given by

$$\begin{aligned} V^{n+1} &= P_+ \left((1 - \sigma_n \epsilon) V^n - \sigma_n (V^n W^n (W^n)^T - X (W^n)^T) \right) \\ W^{n+1} &= P_+ \left((1 - \tau_n \epsilon) W^n - \tau_n ((V^{n+1})^T V^{n+1} W^n - (V^{n+1})^T X) \right), \end{aligned}$$

where P_+ denotes the projection onto the nonnegative orthant; σ_n and τ_n are the step sizes. This update rule can be interpreted as an MM algorithm, due to the nature of projected gradient. Convergence of APG is guaranteed if $\epsilon > 0$, $\sigma_n \leq 1/(2\|W^n (W^n)^T + \epsilon I\|_F^2)$, and $\tau_n \leq 1/(2\|(V^n)^T V^n + \epsilon I\|_F^2)$.

For the distributed implementation, X is assumed to be an $[m] \times p$ matrix. The resulting matrix V is distributed as an $[m] \times r$ matrix, and W is distributed as an $r \times [p]$ matrix. The distributed code is equivalent to replacing `torch.mm` with `distmat.mm` in Listing 4, with an additional optional argument `out_sizes=W.sizes` on Line 10. As discussed in Section 5, distributed matrix multiplication algorithms are automatically selected from Table 1 based on the arguments.

Table 3 shows the performance of the two NMF algorithms on a $[10,000] \times 10,000$ input matrix with various values of r . For APG, $\epsilon = 0$ is used. While the APG algorithm requires more operations per iteration than the multiplicative algorithm, it is faster on CPUs, because subnormal numbers are avoided. As GPU does not slow down with subnormal numbers, each iteration is faster in the multiplicative algorithm. Table 4 shows that APG appears to converge slower early on (10,000 iterations), but it eventually catches up (100,000 iterations) in terms of objective value. As more GPUs are used, the algorithms speed up in general.

TABLE 3
Runtime (in seconds) comparisons for NMF on the simulated $[10,000] \times 10,000$ data

method	r	10,000 iterations				
		CPU	1 GPU	2 GPUs	4 GPUs	8 GPUs
Multiplicative	20	655	160	93	62	50
	40	978	165	102	73	72
	60	1355	168	109	85	86
APG ($\epsilon = 0$)	20	504	164	97	66	57
	40	783	168	106	78	77
	60	1062	174	113	90	92

TABLE 4
Comparison of objective function values for simulated $[10,000] \times 10,000$ data after 10,000 iterations and 100,000 iterations

method	r	10,000 iterations	100,000 iterations
Multiplicative	20	8.270667E+06	8.270009E+06
	40	8.210266E+06	8.208682E+06
	60	8.155084E+06	8.152358E+06
APG ($\epsilon = 0$)	20	8.271248E+06	8.270005E+06
	40	8.210835E+06	8.208452E+06
	60	8.155841E+06	8.151794E+06

The only exception is with 8 GPUs with $r = 60$, where inter-GPU communication overhead dominates the actual computation.

Additional experiments were conducted to see how the value of ϵ affects the convergence. The results are shown in Table 5. Convergence was faster for higher values of ϵ . The number of iterations to convergence in the multiplicative algorithm was longer than the APG with $\epsilon = 10$ for higher-rank decompositions ($r = 40$ and 60) due to heavier communication burden.

Table 6 displays the performance comparison of APG between single-machine multi-GPU and multi-instance virtual cluster settings. The datasets used were of different sizes: “small,” $10,000 \times 10,000$; “mid-size,” $200,000 \times 100,000$; and “large-size,” $200,000 \times 200,000$. For reference, the dataset used in Zhou et al. (2010) was of size 2429×361 . Multi-GPU setting achieved up to 4.14x-speedup over a single CPU instance with the small dataset, but could not run larger datasets. The cluster in a cloud was scalable on larger datasets, running faster with more instances, up to 4.10x-speedup over the two-instance cluster.

6.2. Positron emission tomography

Positron emission tomography (PET) is one of the earliest applications of the EM algorithm in computed tomography (Lange and Carson, 1984; Vardi et al., 1985). In this scenario, we consider a two-dimensional imaging consisted of p pixels obtained from the circular geometry of q photon detectors. We estimate Poisson emission intensities $\lambda = (\lambda_1, \dots, \lambda_p)$, which is proportional to the concentration of radioactively labeled isotopes injected to biomolecules. Such an isotope emits a positron, which collides with a nearby electron, forming two gamma-ray photons flying in almost opposite directions. These two photons are detected by a pair of photon detectors corresponding to the line of flight. The coincidence counts (y_1, \dots, y_d) are observed. Detector pairs are enumerated by $1, 2, \dots, d = q(q-1)/2$. The likelihood of detection for a detector pair i is modeled by Poisson distribution with mean $\sum_{j=1}^p e_{ij} \lambda_j$, where e_{ij} is the probability that a pair of photons is detected by the detector pair i given that a positron is emitted in the pixel location j . The matrix $E = (e_{ij}) \in \mathbb{R}^{d \times p}$ can be precomputed based on the geometry of the detectors. The corresponding loglikelihood to

Table 5: Convergence time comparisons for different values of ϵ in APG and the multiplicative method

Method	$r = 20, 8 \text{ GPUs}$			$r = 40, 8 \text{ GPUs}$			$r = 60, 4 \text{ GPUs}$		
	iterations	time (s)	function	iterations	time (s)	function	iterations	time (s)	function
Multiplicative	21200	110	8.270530E+06	36600	269	8.209031E+06	50000	446	8.152769E+06
APG $\epsilon = 0$	31500	198	8.270202E+06	37400	310	8.208875E+06	55500	536	8.152228E+06
APG $\epsilon = 0.1$	30700	191	8.274285E+06	36700	302	8.210324E+06	55500	537	8.153890E+06
APG $\epsilon = 1$	30500	190	8.282346E+06	37300	307	8.223108E+06	47800	460	8.168503E+06
APG $\epsilon = 10$	28000	178	8.389818E+06	31000	257	8.347859E+06	46400	448	8.308998E+06

Table 6: Runtime of APG algorithm for NMF on simulated data. “x” denotes that the experiment failed due to running out of device memory.

configuration	10000×10000 10,000 iterations			200000×100000 1,000 iterations			200000×200000 1,000 iterations		
	$r = 20$	$r = 40$	$r = 60$	$r = 20$	$r = 40$	$r = 60$	$r = 20$	$r = 40$	$r = 60$
GPUs									
1	164	168	174	x	x	x	x	x	x
2	97	106	113	x	x	x	x	x	x
4	66	78	90	x	x	x	x	x	x
8	57	77	92	x	x	x	x	x	x
AWS EC2 c5.18xlarge instances									
1	236	471	549	x	x	x	x	x	x
2	198	375	493	1487	1589	2074	x	x	x
4	205	310	430	863	998	1233	1493	1908	2232
5	230	340	481	661	896	1082	1326	1652	2070
8	328	390	536	448	541	688	937	1044	1587
10	420	559	643	422	540	682	737	937	1179
20	391	1094	1293	363	489	592	693	818	1041

maximize is given by

$$L(\lambda) = \sum_{i=1}^d \left[y_i \log \left(\sum_{j=1}^p e_{ij} \lambda_j \right) - \sum_{j=1}^p e_{ij} \lambda_j \right].$$

Without a spatial regularization term, the reconstructed intensity map is grainy. One remedy is adding a ridge-type penalty of $-(\mu/2)\|D\lambda\|_2^2$, where D is the finite difference matrix on the pixel grid; each row of D has one $+1$ and one -1 . The MM iteration based on separation of the penalty function by the minorization

$$(\lambda_j - \lambda_k)^2 \geq -\frac{1}{2}(2\lambda_j - \lambda_j^n - \lambda_k^n)^2 - \frac{1}{2}(2\lambda_k - \lambda_j^n - \lambda_k^n)^2$$

is:

$$\begin{aligned} z_{ij}^{n+1} &= e_{ij} y_i \lambda_j^n / \left(\sum_k e_{ik} \lambda_k^n \right) \\ b_j^{n+1} &= \mu \left(n_j \lambda_j^n + \sum_k g_{jk} \lambda_k^n \right) - 1 \\ \lambda_j^{n+1} &= \left(-b_j^{n+1} - \sqrt{(b_j^{n+1})^2 - 4a_j \sum_{i=1}^d z_{ij}^{n+1}} \right) / (2a_j), \end{aligned}$$

where $n_j = \sum_k g_{jk}$ and $a_j = -2\mu n_j$ are precomputed. Matrix $G = (g_{jk})$ is the adjacency matrix corresponding to the grid. See Section 3.2 of [Zhou et al. \(2010\)](#) for the detailed derivation. By using matrix notations and broadcasting semantics, the PyTorch code can be succinctly written as in Listing 5.

```

1 # G: adjacency matrix, sparse p-by-p
2 # mu: roughness penalty parameter
3 # E: detection probability matrix, d-by-p
4 # lambda: poisson intensity, p-by-1, randomly initialized
5 # y: observed data, d-by-1
6 # eps: a small positive number for numerical stability
7 N = torch.mm(G, torch.ones(G.shape[1], 1))
8 a = -2 * mu * N
9 for i in range(max_iter):
10     e1 = torch.mm(E, lambda)
11     g1 = torch.mm(G, lambda)
12     z = E * y * lambda.t() / (e1 + eps)
13     b = mu * (N * lambda + g1) - 1
14     c = z.sum(dim=0).t()
15     # update lambda
16     if mu != 0:
17         lambda = (-b - (b**2 - 4 * a * c).sqrt()) / (2 * a + eps)
18     else:
19         lambda = -c / (b + self.eps)

```

Listing 5: PyTorch code for PET with a squared difference penalty.

Figure 2 shows the results with a $p = 64 \times 64$ Roland-Varadhan-Frangakis (RVF) phantom ([Roland et al., 2007](#)) with $d = 2016$ with various values of μ , and Figure 4 shows the results

TABLE 7

Convergence time comparisons for TV-penalized PET with different values of ρ . Problem dimension is $p = 10,000$ and $d = 16,110$. Eight GPUs were used.

ρ	iterations	time (s)	function
0	6400	20.6	-2.417200E+05
0.01	4900	15.8	-2.412787E+05
0.1	5000	16.1	-2.390336E+05
1	2800	9.5	-2.212579E+05

with a 128×128 extended cardiac-torso (XCAT) phantom (Lim et al., 2018; Ryu et al., 2019+) with $d = 8128$. Images get smooth as the value of μ increases, but the edges are blurry.

To promote sharp contrast, the total variation (TV) penalty (Rudin et al., 1992) can be employed. Adding an anisotropic TV penalty yields minimizing

$$-L(\lambda) + \rho \|D\lambda\|_1 = \sum_{i=1}^d [(E\lambda)_i - y_i \log((E\lambda)_i)] + \rho \|D\lambda\|_1.$$

We can use the PDHG algorithm discussed in Section 4.3. Put $K = [E^T, D^T]^T$, $f(z, w) = \sum_i (-y_i \log z_i) + \rho \|w\|_1$, and $g(\lambda) = \mathbf{1}^T E\lambda + \delta_+(\lambda)$, where $\mathbf{1}$ is the all-one vector of conforming shape and δ_+ is the $0/\infty$ indicator function for the nonnegative orthant. Since $f(z, w)$ is separable in z and w , applying iteration (4) using the proximity operator (2), we obtain the following update rule:

$$\begin{aligned} \lambda^{n+1} &= P_+(\lambda^n - \tau(E^T z + D^T w + E^T \mathbf{1})) \\ \tilde{\lambda}^{n+1} &= 2\lambda^{n+1} - \lambda^n \\ z^{n+1} &= \frac{1}{2} \left((z^n + \sigma E \tilde{\lambda}^{n+1}) - \sqrt{(z^n + \sigma E \tilde{\lambda}^{n+1})^2 + 4\sigma y} \right) \\ w^{n+1} &= P_{[-\rho, \rho]}(w^n + \sigma D \tilde{\lambda}^{n+1}), \end{aligned}$$

where $P_{[-\rho, \rho]}$ is elementwise projection to the interval $[-\rho, \rho]$. Convergence is guaranteed if $\sigma\tau < 1/\| [ED] \|_2^2$.

Figures 3 and 5 are the TV-reconstructed versions of Figures 2 and 4, respectively. Compare the edge contrast. Table 7 shows the convergence with different values of penalty parameters. Observe that the algorithm converges faster for large values of ρ . Scalability experiments were carried out with large RVF-like phantoms using grid sizes $p = 300 \times 300$, 400×400 , and 900×900 , with the number of detectors $q = 600$ ($d = 179, 700$). The matrix E is distributed as a $d \times [p]$ matrix, and the matrix D is distributed as an $l \times [p]$ matrix. The symmetric adjacency matrix G is distributed as a $[p] \times p$ matrix. The sparse structure of these matrices is exploited using the sparse tensor data structure of PyTorch. Timing per 1000 iterations is reported in Table 8. For reference, the data used in Zhou et al. (2010) was for 64×64 grid with $q = 64$, or $d = 2016$. Time per iterations of the PDHG method for the TV penalty is noticeably shorter as each iteration is much simpler than the MM counterpart for the ridge penalty, with no intermediate matrix created. The total elapsed time gets shorter with more GPUs. Although the speedup when adding more devices is somewhat mitigated in this case due to using sparse structure, resulting in 1.25x-speedup for 8 GPUs over 2 GPUs with $p = 160,000$, we can still take advantage of the scalability of memory with more devices.

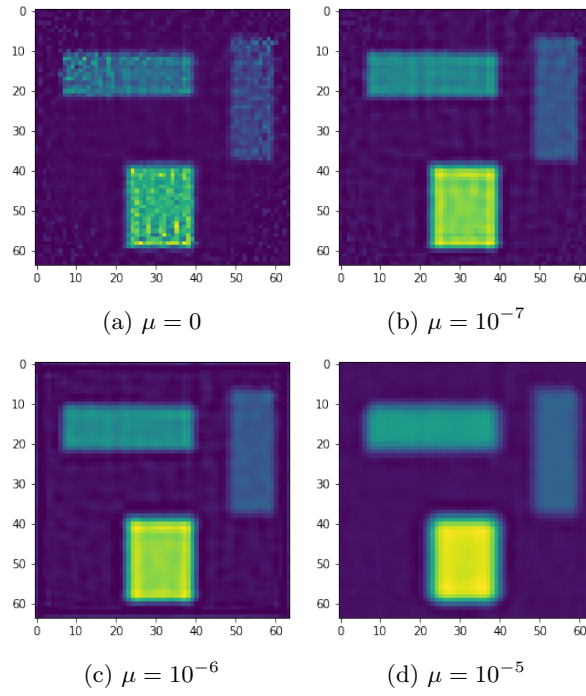


Fig 2: Reconstructed images of the RVF phantom with a ridge penalty.

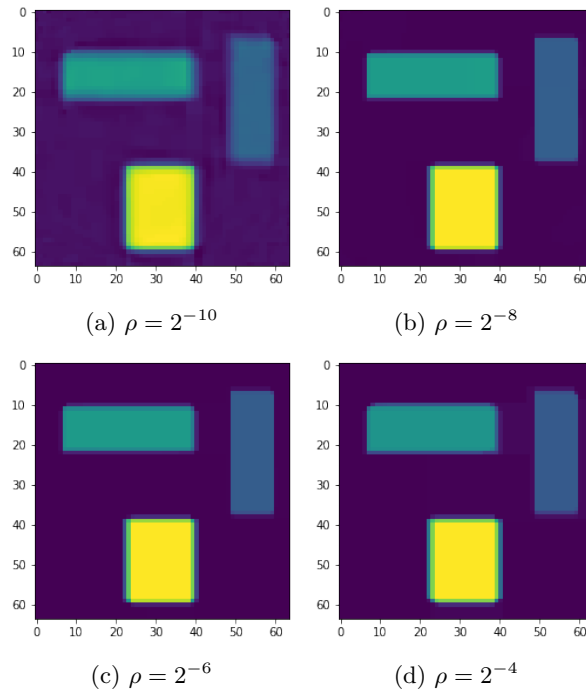


Fig 3: Reconstructed images of the RVF phantom with a TV penalty.

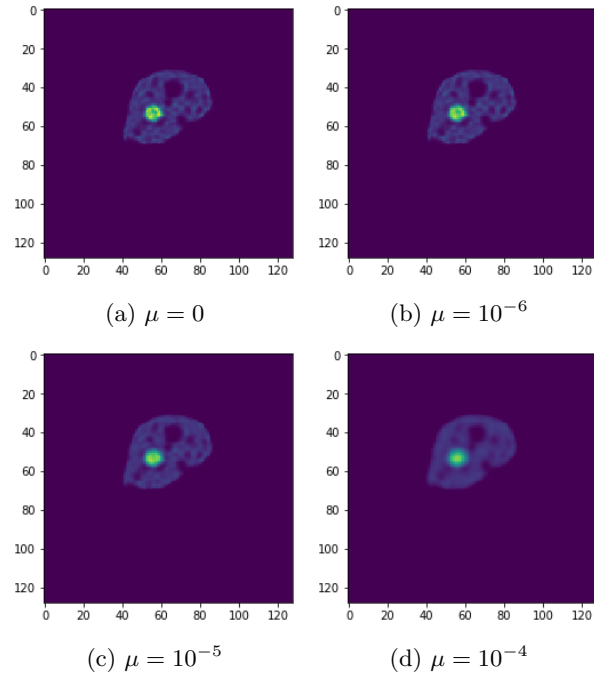


Fig 4: Reconstructed images of the XCAT phantom with a ridge penalty.

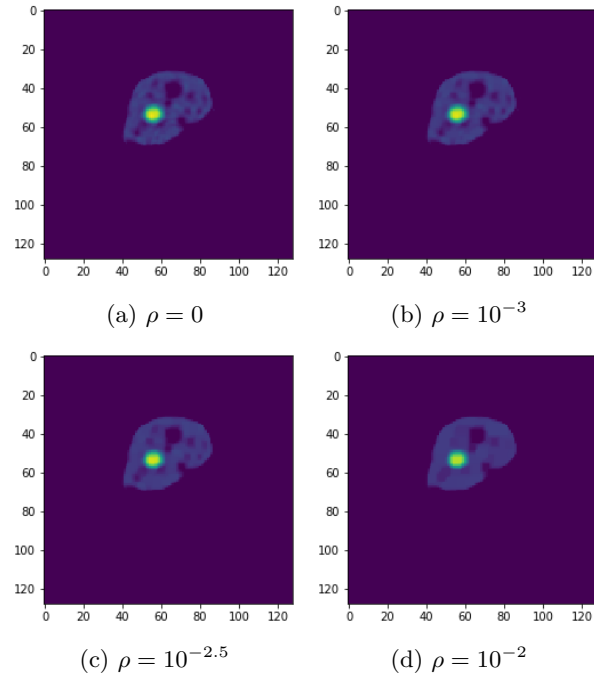


Fig 5: Reconstructed images of the XCAT phantom with a TV penalty.

TABLE 8

Runtime (in seconds) comparison of 1,000 iterations of absolute-value penalized PET. We exploited sparse structures of E and D . The number of detector pairs d was fixed at 179,700.

configuration	$p = 90,000$	$p = 160,000$	$p = 810,000$
GPUs			
1	×	×	×
2	21	35	×
4	19	31	×
8	18	28	×
AWS EC2 c5.18xlarge instances			
1	63	108	530
2	46	84	381
4	36	49	210
5	36	45	188
8	33	39	178
10	38	37	153
20	26	28	131

6.3. Multidimensional scaling

Multidimensional scaling is one of the earliest applications of the MM principle (de Leeuw, 1977; de Leeuw and Heiser, 1977). In this example, we reduce the dimensionality of m data points by mapping them into $\theta = (\theta_1, \dots, \theta_m)^T \in \mathbb{R}^{[m] \times q}$ in q -dimensional Euclidean space in a way that keeps the dissimilarity measure y_{ij} between the data points x_i and x_j as close as possible to that in the original manifold. In other words, we minimize the stress function

$$\begin{aligned} f(\theta) &= \sum_{i=1}^q \sum_{j \neq i} w_{ij} (y_{ij} - \|\theta_i - \theta_j\|_2)^2 \\ &= \sum_{i=1}^q \sum_{j \neq i} [-2w_{ij}y_{ij}\|\theta_i - \theta_j\|_2 + w_{ij}\|\theta_i - \theta_j\|_2^2] + \text{const.}, \end{aligned}$$

where the w_{ij} are the weights. We adopt the following surrogate function that majorizes f :

$$g(\theta|\theta^n) = 2 \sum_{i=1}^q \sum_{j \neq i} \left[w_{ij} \left\| \theta_i - \frac{1}{2}(\theta_i^n + \theta_j^n) \right\|_2^2 - \frac{w_{ij}y_{ij}(\theta_i)^T(\theta_i^n - \theta_j^n)}{\|\theta_i^n - \theta_j^n\|_2} \right].$$

The corresponding update equation obtained from setting the gradient of $g(\theta|\theta^n)$ to zero is

$$\theta_{ik}^{n+1} = \left(\sum_{j \neq i} \left[y_{ij} \frac{\theta_{ik}^n - \theta_{jk}^n}{\|\theta_i^n - \theta_j^n\|_2} + (\theta_{ik}^n + \theta_{jk}^n) \right] \right) / \left(2 \sum_{j \neq i} w_{ij} \right)$$

for $i = 1, \dots, n$ and $k = 1, \dots, q$. We refer the readers to Zhou et al. (2010) for the detailed derivation. In PyTorch syntax, this can be parallelly computed by the code in Listing 6. For numerical experiments, we sampled a $[10,000] \times 10,000$ and a $[100,000] \times 1,000$ dataset from the standard normal distribution. For reference, the dataset used in Zhou et al. (2010) was 401×401 . The pairwise Euclidean distances between data points were computed distributedly (Li et al., 2010): in each stage, data on one of the processors are broadcast and each processor computes pairwise distances between the data residing on its memory and the broadcast data. This is repeated until all the processors broadcast its data. The dimension of the datapoints does not matter after computing the pairwise distances. Elapsed time is reported in Table 9. For $q = 20$, the eight-GPU setting achieves 5.32x-speedup compared to a single 36-core CPU AWS instance and 6.13x-speedup compared to a single GPU.

```

1 # initialize theta from Unif(-1, 1)
2 for i in range(max_iter):
3     # compute Z_{ij} = y_{ij} / (|\theta^i - \theta^j|_2^2)
4     d = torch.mm(self.theta, self.theta.t())
5     TtT_diag = torch.diag(d).view(-1, 1) # to broadcast it
6     d = d.mul_(-2.0)
7     d.add_(TtT_diag)
8     d.add_(TtT_diag.t())
9     # directly modify the diagonal
10    d_diag = d.view(-1)[:(self.q+1)]
11    d_diag.fill_(inf)
12    Z = torch.div(self.y, d)
13    Z_sums = Z.sum(dim=1, keepdim=True) # length-q vector
14
15    # Compute \theta^T (W - Z_n), where W = 1 - diag(1,1,...1)
16    weight_minus_Z = 1.0 - Z
17    weight_minus_Z_diag = WmZ.view(-1)[:(self.q+1)]
18    weight_minus_Z_diag.fill_(0) # directly modify the diagonal where the weight is
19    zero
20    TWmZ = torch.mm(self.theta.t(), weight_minus_Z)
21
22    theta = (self.theta * (self.w_sums + Z_sums) + TWmZ.t()) / (self.w_sums * 2.0)

```

Listing 6: PyTorch code for MDS.

Now consider a much bigger dataset with 100,000 samples. This involves storing the distance matrix of size $[100,000] \times 100,000$, which takes 74.5 GB of the memory. It was impossible to run the experiment on GPUs due to the memory limits. On the other hand, we observed 3.78x-speedup with 20 instances (720 cores) with respect to four instances (144 cores) of CPU nodes.

6.4. ℓ_1 -regularized Cox regression

Finally, we apply the proximal gradient descent to ℓ_1 -regularized Cox regression (Cox, 1972). In this problem, we are given a covariate matrix $X \in \mathbb{R}^{m \times p}$, and a possibly right-censored survival time $y = (y_1, \dots, y_m)$ as data. Each element of y is defined by $y_i = \min\{t_i, c_i\}$, where t_i is time to event and c_i is right-censoring time for that sample. $\delta_i = I_{\{t_i \leq c_i\}}$ indicates if the sample i is censored or not. We put $\delta = (\delta_1, \dots, \delta_m)^T$. The log partial likelihood of the Cox model is then

$$L(\beta) = \sum_{i=1}^m \delta_i \left[\beta^T x_i - \log \left(\sum_{j: y_j \geq y_i} \exp(\beta^T x_j) \right) \right].$$

Coordinate descent-type approaches for this type of analyses are proposed by Suchard et al. (2013) and Mittal et al. (2014).

To obtain a proximal gradient update, we need the gradient $\nabla L(\beta)$ and its Lipschitz constant. The gradient of the log partial likelihood is

$$\nabla L(\beta) = X^T (I - P) \delta,$$

where we define $w_i = \exp(x_i^T \beta)$, $W_j = \sum_{i: y_i \geq y_j} w_i$, and the matrix $P = (\pi_{ij})$ whose elements are

$$\pi_{ij} = I(y_i \geq y_j) w_i / W_j.$$

TABLE 9
Runtimes (in seconds) of 1000 iterations for MDS.

configuration	10,000 datapoints 10,000 iterations			100,000 datapoints 1,000 iterations		
	$q = 20$	$q = 40$	$q = 60$	$q = 20$	$q = 40$	$q = 60$
	GPUs					
1	368	376	384	×	×	×
2	185	190	195	×	×	×
4	100	103	108	×	×	×
8	60	67	73	×	×	×
AWS EC2 c5.18xlarge instances						
1	1428	1427	1424	×	×	×
2	734	837	801	×	×	×
4	424	568	596	3103	3470	3296
5	364	406	547	2634	2700	2730
8	350	425	520	1580	1794	1834
10	275	414	457	1490	1454	1558
20	319	440	511	820	958	1043

Each row of P is normalized to sum to one. A Lipschitz constant of $\nabla L(\beta)$ can be found by finding an upper bound of $\|\nabla^2 L(\beta)\|_2$, where $\nabla^2 L(\beta)$ is the Hessian of $L(\beta)$:

$$\nabla^2 L(\beta) = X^T (P \text{diag}(\delta) P^T - \text{diag}(P\delta)) X.$$

Note $\|P\|_2 \leq 1$, since the sum of each row of P is 1. It follows that $\|\nabla^2 L(\beta)\|_2 \leq 2\|X\|_2^2$, and $\|X\|_2$ can be quickly computed by using the power iteration (Golub and Van Loan, 2013).

We introduce an ℓ_1 -penalty to the log partial likelihood in order to enforce sparsity in the regression coefficients and use the proximal gradient descent to estimate β by putting $g(\beta) = -L(\beta)$, $f(\beta) = \lambda\|\beta\|_1$. Then the update rule is:

$$\begin{aligned} w_i^{n+1} &= \exp(x_i^T \beta); \quad W_j^{n+1} = \sum_{i: y_i \geq y_j} w_i^{n+1} \\ \pi_{ij}^{n+1} &= I(t_i \geq t_j) w_i^{n+1} / W_j^{n+1} \\ \Delta^{n+1} &= X^T (I - P^{n+1}) \delta, \quad \text{where } P^{n+1} = (\pi_{ij}^{n+1}) \\ \beta^{n+1} &= \mathcal{S}_\lambda(\beta^n + \sigma \Delta^{n+1}). \end{aligned}$$

If the data are sorted in the nonincreasing order of y_i , W_j^n can be computed using the cumulative sum function. While this is not so obvious to implement in a parallel environment, a CUDA device kernel function for this operation is readily provided with PyTorch. We can write a simple proximal gradient descent update for the Cox regression as in Listing 7, assuming no ties in y_i 's for simplicity. The soft-thresholding operator $\mathcal{S}_\lambda(x)$ is also implemented in PyTorch. We compute the full w_i/W_j first with `w / W.t()` then multiply it to the indicator $I(y_i \geq y_j)$ precomputed.

For simulation, the data matrix $X \in \mathbb{R}^{m \times [p]}$, distributed along the columns, is sampled from the standard normal distribution. The algorithm is designed to keep a copy of the estimand β in every device. All the numerical experiments were carried out with double-precision even for GPUs, for the following reason. For a very small value of λ (we used $\lambda = 10^{-5}$), when single-precision is used in GPUs, the estimate quickly tended to “not a number (NaN)”s due to numerical instability of the CUDA kernel. Double-precision did not generate such a problem. Although desktop GPU models such as Nvidia GTX and Titan X are not optimized for double-precision floating-point operations and is known to be 32 times slower for double-precision operations than single-precision operations, this does not

```

1 # X: data matrix, m-by-p
2 # delta: censoring indicator, m-by-1
3 # y: right-censored survival time
4 # X is assumed to be sorted in decreasing order of y_i
5 # lambda: penalty parameter
6
7 soft_threshold = torch.nn.Softshrink(lambda)
8 L = 2 * power(X) ** 2 # power(X): power iteration to compute the spectral norm of X
9 sigma = 1/L
10
11 # mask: pi_ind[i, j] = (y[i] >= y[j])
12 pi_ind = (y - y.t()) >= 0).to(dtype=tf.float64)
13
14 for i in range(max_iter):
15     Xbeta = torch.mm(X, beta)
16     w = torch.exp(Xbeta)
17     W = w.cumsum(0)
18     pi = (w / W.t()) * pi_ind
19     grad = torch.mm(X.t(), delta - torch.mm(pi, delta))
20     beta = soft_threshold(beta + grad * sigma)

```

Listing 7: PyTorch code for proximal gradient descent on ℓ_1 -regularized Cox regression. power indicates the power method to compute maximum singular value.

necessarily mean that the total computation time is 32 times slower because latency takes a significant portion of the total computation time in GPU computing.

In order to demonstrate the scalability of the algorithm, elapsed times for $10,000 \times [10,000]$ and $100,000 \times [200,000]$ simulated data are reported in Table 10. We can see 3.92x speedup from 4 nodes to 20 nodes in the virtual cluster. Even with double-precision arithmetics, eight GPUs could achieve a 6.30x-speedup over the single 36-core CPU instance. Once again, virtual clusters in a cloud exhibited better scalability.

TABLE 10
Runtime comparison of ℓ_1 -regularized Cox regression over multi-node virtual cluster on AWS EC2.
Elapsed time (in seconds) after 1,000 iterations.

configuration	10,000 × [10,000] 10,000 iterations	100,000 × [200,000] 1,000 iterations
GPUs		
1	386	×
2	204	×
4	123	×
8	92	×
AWS EC2 c5.18xlarge instances		
1	580	×
2	309	×
4	217	1507
5	170	1535
8	145	775
10	132	617
20	148	384

6.5. Genome-wide survival analysis of the UK Biobank dataset

We demonstrate a real-world application of ℓ_1 -regularized Cox regression to genome-wide survival analysis for Type 2 Diabetes (T2D). We used a UK Biobank dataset (Sudlow et al., 2015) that contains information on approximately 800,000 single nucleotide polymorphisms (SNPs) of 500,000 individual subjects recruited from the United Kingdom. After filtering SNPs for quality control and subjects for the exclusion of Type 1 Diabetes patients, 402,297 subjects including 17,994 T2D patients and 470,189 SNPs remained. We randomly sampled 200,000 subjects including 8,995 T2D patients for our analysis. Any missing genotypes were imputed with the column mean. Along with the SNPs, sex and top ten principal components were included as unpenalized covariates to adjust for population-specific variations. The resulting dataset was 701 GB with double-precision.

The analysis for this large-scale genome-wide dataset was conducted as follows. Incidence of T2D was used as the event ($\delta_i = 1$) and the age of onset was used as survival time y_i . For non-T2D subjects ($\delta_i = 0$), age at the last visit was used as y_i . We chose 63 different values of the regularization parameter λ in the range $[0.7 \times 10^{-9}, 1.6 \times 10^{-8}]$, with which 0 to 111 SNPs were selected. For each value of λ , the ℓ_1 -regularized Cox regression model of Section 6.4 was fitted. Every run converged after at most 2080 iterations that took less than 2800 seconds using 20 `c5.18xlarge` instances from AWS EC2.

The SNPs are ranked based on the largest value of λ for which each SNP is selected. (No variables were removed once selected within the range of λ used. The regularization path and the full list of the selected SNPs are available in Appendix D.) Among the 111 SNPs selected, three of the top four selections are located on TCF7L2, whose association with T2D is well-known (Scott et al., 2007; The Wellcome Trust Case Control Consortium, 2007). Also prominently selected are SNPs from genes SLC45A2 and HERC2, whose variants are known to be associated with skin, eye, and hair pigmentation (Cook et al., 2009). This is possibly due to the dominantly European population in the UK Biobank study. Mapped genes for 24 SNPs out of the selected 111 were also reported in Mahajan et al. (2018), a meta-analysis of 32 genome-wide association studies (GWAS) for about 898,130 individuals of European ancestry; see Tables D.1 and D.2 for details. We then conducted an unpenalized Cox regression analysis using the 111 selected SNPs. The nine SNPs with the p -values less than 0.01 are listed in Table 11. The locations in Table 11 are with respect to the reference genome GRCh37 (Church et al., 2011), and mapped genes were predicted by the Ensembl Variant Effect Predictor (McLaren et al., 2016). Among these nine SNPs, three of them were directly shown to be associated with T2D (The Wellcome Trust Case Control Consortium (2007) and Dupuis et al. (2010) for rs4506565, Voight et al. (2010) for rs8042680, Ng et al. (2014) for rs343092). Three other SNPs have mapped genes reported to be associated with T2D in Mahajan et al. (2018): rs12243326 on TCF7L2, rs343092 on HMGA2, and rs231354 on KCNQ1.

Although the interpretation of the results requires additional sub-analysis, the result shows the promise of joint association analysis using multiple regression models. In GWAS it is customary to analyze the data on SNP-by-SNP basis. Among the mapped genes harboring the 111 SNPs selected by our half-million-variate regression analysis are CPLX3 and CACNA1A, associated with regulation of insulin secretion, and SEMA7A and HLA-DRA involved with inflammatory responses (based on DAVID (Huang et al., 2009a,b)). These genes might have been missed in conventional univariate analysis of T2D due to moderate statistical significance values. Joint GWAS may overcome such a limitation, and is possible by combining the computing power of modern HPC and scalable algorithms.

TABLE 11
SNPs with p-values of less than 0.01 on unpenalized Cox regression with variables selected by ℓ_1 -penalized Cox regression

SNP ID	Chr.	Location	A1 ^A	A2 ^B	MAF ^C	Mapped Gene	Coefficient	p-value
rs4506565	10	114756041	A	T	0.238	TCF7L2	2.810e-1	<2e-16
rs12243326	10	114788815	C	T	0.249	TCF7L2	1.963e-1	0.003467
rs8042680	15	91521337	A	C	0.277	PRC1	2.667e-1	0.005052
rs343092	12	66250940	T	G	0.463	HMGA2	-7.204e-2	0.000400
rs7899137	10	76668462	A	C	0.289	KAT6B	-4.776e-2	0.002166
rs8180897	8	121699907	A	G	0.445	SNTB1	6.361e-2	0.000149
rs10416717	19	13521528	A	G	0.470	CACNA1A	5.965e-2	0.009474
rs231354	11	2706351	C	T	0.329	KCNQ1	4.861e-2	0.001604
rs9268644	6	32408044	C	A	0.282	HLA-DRA	6.589e-2	2.11e-5

^A Minor allele, ^B Major allele, ^C Minor allele frequency. The boldface indicates the risk allele determined by the reference allele and the sign of the regression coefficient.

7. Discussion

Abstractions of highly complex computing operations have rapidly evolved over the last decade. In this article, we have explained how statisticians can benefit from this evolution. We have seen how deep learning technology is relevant to high-performance statistical computing. We have also seen that many useful tools to incorporate computing clusters and accelerators have been created. Unfortunately, such developments have been mainly made in languages other than R, particularly in Python, with which statisticians might not be familiar with. Although there are libraries that deal with simple parallel computation in R, common issues with these libraries are that they are difficult to incorporate GPUs which might significantly speed up the computation and that it is hard to write more full-fledged parallel programs without directly writing code in C or C++. This two-language problem calls for statisticians to take a second look at Python. Fortunately, this language is not hard to learn, and younger generations are quite familiar with it. A remedy from the R side may be either developing more user-friendly interfaces for the distributed-memory environment, with help from those who are engaged in computer engineering, or R community writing a good wrapper for the important Python libraries. A good starting point may be a Python interface to R. The R package `reticulate` (Ushey et al., 2019), might be a good candidate. For example, there is an interface to TensorFlow based on `reticulate` (RStudio, n.d.).

The methods discussed in this article can be applied efficiently even when the dataset is larger than several gigabytes by using multiple CPU machines or using multiple GPUs. The advantages of using multiple CPU machines and multiple GPUs are two-fold. First, we can take advantage of data parallelism with more computing cores, accelerating the computation. Second, we can push the upper limit of the size of the dataset to analyze. As cloud providers now support virtual clusters better suited for HPC, statisticians can deal with bigger problems utilizing such services, using up to several thousand cores easily.

A major weakness of the current approach is that its effectiveness can be degraded by the communication cost between the nodes and devices. One way to avoid this issue is by using high-speed interconnection between the nodes and devices. With multi-CPU machines, it can be covered by a high-speed interconnection technology such as InfiniBand. Even when such kind of environment is not affordable, we may still use relatively high-speed connection equipped with instances from a cloud. The network bandwidth of 25Gbps supported for `c5.18xlarge` instances of AWS was quite effective in our experiments. Another way to alleviate the communication issue is employing a communication-avoiding algorithm (Van De Geijn and Watts, 1997; Ballard et al., 2011; Koanantakool et al., 2016) to minimize the

amount of communication between computing units. This approach was utilized for statistical inference (Jordan et al., 2019) and sparse inverse covariance estimation (Koanantakool et al., 2018).

Loss of accuracy due to the single-precision of the GPU, prominent in our Cox regression example, can be solved by purchasing scientifically-oriented GPUs with better double-precision supports, which costs money. Another option is to go to clouds: for example, P2 and P3 instances in AWS support scientific GPUs. Nevertheless, even with that double-precision floating-point operation speed is 1/32 compared to single-precision, desktop GPUs with double-precision could achieve more than 10-fold speedup over CPU.

Although PyTorch has been advocated throughout this article, it is not the only path towards the easy-to-use programming model in shared- and distributed-memory programming environments. A possible alternative is Julia (Bezanson et al., 2017). Julia uses the concept of multiple dispatch, which makes it more flexible to deal with data in many different forms. The data might be arrays of various types, such as half-precision, single-precision, double-precision, 32-bit integer, and 64-bit integer. In addition, the data can reside in a wide variety of environments, such as GPUs (Besard et al., 2018) and multiple CPU nodes implementing the distributed memory model (JuliaParallel Team, n.d.; Janssens, n.d.). Operations in these HPC environments can be overloaded on conventional arithmetic, thanks to the highly flexible multiple dispatch feature of the language: write code once, operate on all these environments. While its 1.0 release in August 2018 is still fresh, Julia has the potential to be a powerful tool for HPC for statisticians once the platforms and user community gets more mature.

References

- Abadi, M., Agarwal, A., Barham, P., Brevdo, E., Chen, Z., Citro, C., Corrado, G. S., Davis, A., Dean, J., Devin, M., Ghemawat, S., Goodfellow, I., Harp, A., Irving, G., Isard, M., Jia, Y., Jozefowicz, R., Kaiser, L., Kudlur, M., Levenberg, J., Mané, D., Monga, R., Moore, S., Murray, D., Olah, C., Schuster, M., Shlens, J., Steiner, B., Sutskever, I., Talwar, K., Tucker, P., Vanhoucke, V., Vasudevan, V., Viégas, F., Vinyals, O., Warden, P., Wattenberg, M., Wicke, M., Yu, Y. and Zheng, X. (2016), ‘TensorFlow: Large-scale machine learning on heterogeneous systems’, *arXiv preprint arXiv:1603.04467*.
- URL:** <http://tensorflow.org/>
- Amazon Web Services (n.d.), ‘AWS ParallelCluster documentation’. Accessed: 2019-10-14.
- URL:** <https://docs.aws.amazon.com/parallelcluster/index.html>
- Armbrust, M., Fox, A., Griffith, R., Joseph, A. D., Katz, R., Konwinski, A., Lee, G., Patterson, D., Rabkin, A., Stoica, I. and Zaharia, M. (2010), ‘A view of cloud computing’, *Commun. ACM* **53**(4), 50–58.
- Bahrampour, S., Ramakrishnan, N., Schott, L. and Shah, M. (2015), ‘Comparative study of deep learning software frameworks’, *arXiv preprint arXiv:1511.06435*.
- Ballard, G., Demmel, J., Holtz, O. and Schwartz, O. (2011), ‘Minimizing communication in numerical linear algebra’, *SIAM Journal on Matrix Analysis and Applications* **32**(3), 866–901.
- Bauschke, H. H. and Combettes, P. L. (2011), *Convex analysis and monotone operator theory in Hilbert spaces*, Springer Science & Business Media.
- Beck, A. (2017), *First-order methods in optimization*, SIAM.
- Beck, A. and Teboulle, M. (2009), ‘A fast iterative shrinkage-thresholding algorithm for linear inverse problems’, *SIAM Journal on Imaging Sciences* **2**(1), 183–202.
- Bergstra, J., Bastien, F., Breuleux, O., Lamblin, P., Pascanu, R., Delalleau, O., Desjardins, G., Warde-Farley, D., Goodfellow, I., Bergeron, A. et al. (2011), Theano: Deep learning

- on GPUs with Python, in ‘NIPS 2011, BigLearning Workshop, Granada, Spain’, Vol. 3, pp. 1–48.
- Besard, T., Foket, C. and De Sutter, B. (2018), ‘Effective extensible programming: Unleashing Julia on GPUs’, *IEEE Transactions on Parallel and Distributed Systems* .
- Bezanson, J., Edelman, A., Karpinski, S. and Shah, V. B. (2017), ‘Julia: A fresh approach to numerical computing’, *SIAM Review* **59**(1), 65–98.
- Blackford, L. S., Petitet, A., Pozo, R., Remington, K., Whaley, R. C., Demmel, J., Dongarra, J., Duff, I., Hammarling, S., Henry, G. et al. (2002), ‘An updated set of basic linear algebra subprograms (BLAS)’, *ACM Transactions on Mathematical Software* **28**(2), 135–151.
- Boyd, S., Parikh, N., Chu, E., Peleato, B. and Eckstein, J. (2010), ‘Distributed optimization and statistical learning via the alternating direction method of multipliers’, *Foundations and Trends in Machine Learning* .
- Buckner, J., Wilson, J., Seligman, M., Athey, B., Watson, S. and Meng, F. (2009), ‘The gputools package enables GPU computing in R’, *Bioinformatics* **26**(1), 134–135.
- Chambolle, A. and Pock, T. (2011), ‘A first-order primal-dual algorithm for convex problems with applications to imaging’, *Journal of Mathematical Imaging and Vision* **40**(1), 120–145.
- Chen, T., Li, M., Li, Y., Lin, M., Wang, N., Wang, M., Xiao, T., Xu, B., Zhang, C. and Zhang, Z. (2015), ‘MXNet: A flexible and efficient machine learning library for heterogeneous distributed systems’, *arXiv preprint arXiv:1512.01274* .
- Cheng, B. and Titterton, D. M. (1994), ‘Neural networks: A review from a statistical perspective’, *Statistical Science* pp. 2–30.
- Chi, E. C., Zhou, H. and Lange, K. (2014), ‘Distance majorization and its applications’, *Mathematical Programming* **146**(1-2), 409–436.
- Church, D. M., Schneider, V. A., Graves, T., Auger, K., Cunningham, F., Bouk, N., Chen, H.-C., Agarwala, R., McLaren, W. M., Ritchie, G. R. et al. (2011), ‘Modernizing reference genome assemblies’, *PLoS Biology* **9**(7), e1001091.
- Collobert, R., Kavukcuoglu, K. and Farabet, C. (2011), Torch7: A Matlab-like environment for machine learning, in ‘BigLearn, NIPS workshop’, number EPFL-CONF-192376.
- Combettes, P. L. (2018), ‘Monotone operator theory in convex optimization’, *Mathematical Programming* **170**, 177–206.
- Combettes, P. L. and Pesquet, J.-C. (2011), Proximal splitting methods in signal processing, in ‘Fixed-point algorithms for inverse problems in science and engineering’, Springer, pp. 185–212.
- Condat, L. (2013), ‘A primal-dual splitting method for convex optimization involving Lipschitzian, proximable and linear composite terms’, *Journal of Optimization Theory and Applications* **158**(2), 460–479.
- Cook, A. L., Chen, W., Thurber, A. E., Smit, D. J., Smith, A. G., Bladen, T. G., Brown, D. L., Duffy, D. L., Pastorino, L., Bianchi-Scarra, G. et al. (2009), ‘Analysis of cultured human melanocytes based on polymorphisms within the SLC45A2/MATP, SLC24A5/NCKX5, and OCA2/P loci’, *Journal of Investigative Dermatology* **129**(2), 392–405.
- Cox, D. R. (1972), ‘Regression models and life-tables’, *Journal of the Royal Statistical Society: Series B (Methodological)* **34**(2), 187–202.
- de Leeuw, J. (1977), Applications of convex analysis to multidimensional scaling, in ‘Recent Developments in Statistics (Proc. European Meeting of Statisticians, Grenoble, 1976)’, pp. 133–145.
- de Leeuw, J. and Heiser, W. J. (1977), ‘Convergence of correction matrix algorithms for multidimensional scaling’, *Geometric Representations of Relational Data* pp. 735–752.
- Dempster, A. P., Laird, N. M. and Rubin, D. B. (1977), ‘Maximum likelihood from in-

- complete data via the EM algorithm’, *Journal of the Royal Statistical Society. Series B (methodological)* pp. 1–38.
- Donoho, D. (2017), ‘50 years of data science’, *Journal of Computational and Graphical Statistics* **26**(4), 745–766.
- Dupuis, J., Langenberg, C., Prokopenko, I., Saxena, R., Soranzo, N., Jackson, A. U., Wheeler, E., Glazer, N. L., Bouatia-Naji, N., Gloyn, A. L. et al. (2010), ‘New genetic loci implicated in fasting glucose homeostasis and their impact on type 2 diabetes risk’, *Nature Genetics* **42**(2), 105.
- Eijkhout, V. (2016), *Introduction to High Performance Scientific Computing*, 2nd edn, Lulu.com.
- Esser, E., Zhang, X. and Chan, T. F. (2010), ‘A general framework for a class of first order primal-dual algorithms for convex optimization in imaging science’, *SIAM Journal on Imaging Sciences* **3**(4), 1015–1046.
- Evangelinos, C. and Hill, C. N. (2008), Cloud computing for parallel scientific HPC applications: Feasibility of running coupled atmosphere-ocean climate models on Amazons EC2, in ‘In The 1st Workshop on Cloud Computing and its Applications (CCA)’.
- Fox, A. (2011), ‘Cloud computing What’s in it for me as a scientist?’, *Science* **331**(6016), 406–407.
- Friedman, J., Hastie, T. and Tibshirani, R. (2010), ‘Regularization paths for generalized linear models via coordinate descent’, *Journal of Statistical Software* **33**(1), 1–22.
- Gabay, D. and Mercier, B. (1976), ‘A dual algorithm for the solution of nonlinear variational problems via finite element approximation’, *Computers & Mathematics with Applications* **2**(1), 17–40.
- Gabriel, E., Fagg, G. E., Bosilca, G., Angskun, T., Dongarra, J. J., Squyres, J. M., Sahay, V., Kambadur, P., Barrett, B., Lumsdaine, A., Castain, R. H., Daniel, D. J., Graham, R. L. and Woodall, T. S. (2004), Open MPI: Goals, concept, and design of a next generation MPI implementation, in ‘Proceedings, 11th European PVM/MPI Users’ Group Meeting’, Budapest, Hungary, pp. 97–104.
- Gentzsch, W. (2001), Sun Grid Engine: Towards creating a compute power grid, in ‘Proceedings First IEEE/ACM International Symposium on Cluster Computing and the Grid’, IEEE, pp. 35–36.
- Glowinski, R. and Marroco, A. (1975), ‘Sur l’approximation, par lments finis d’ordre un, et la rsolution, par pnalisation-dualit d’une classe de problmes de dirichlet non linaires’, *Revue franaise d’automatique, informatique, recherche oprationnelle. Analyse numrique* **9**(2), 41–76.
- Golub, G. H. and Van Loan, C. F. (2013), *Matrix Computations*, Johns Hopkins University Press, Baltimore, MD.
- Gu, Y., Fan, J., Kong, L., Ma, S. and Zou, H. (2018), ‘ADMM for high-dimensional sparse penalized quantile regression’, *Technometrics* **60**(3), 319–331.
- Hager, G. and Wellein, G. (2010), *Introduction to High Performance Computing for Scientists and Engineers*, CRC Press.
- Huang, D. W., Sherman, B. T. and Lempicki, R. A. (2009a), ‘Bioinformatics enrichment tools: paths toward the comprehensive functional analysis of large gene lists’, *Nucleic Acids Research* **37**(1), 1–13.
- Huang, D. W., Sherman, B. T. and Lempicki, R. A. (2009b), ‘Systematic and integrative analysis of large gene lists using DAVID bioinformatics resources’, *Nature Protocols* **4**(1), 44.
- Hunter, D. and Li, R. (2005), ‘Variable selection using MM algorithms’, *The Annals of Statistics* **33**(4), 1617–1642.
- Hunter, D. R. and Lange, K. (2004), ‘A tutorial on MM algorithms’, *The American Statistician* **58**(1), 30–37.

- Hyperion Research (2019), Hyperion Research HPC market update from ISC 2019, Technical report, Hyperion Research.
- IEEE Standards Committee (2008), ‘754-2008 iee standard for floating-point arithmetic’, *IEEE Computer Society Std* **2008**, 517.
- Janssens, B. (n.d.), ‘MPIArrays.jl: Distributed arrays based on MPI onesided communication’. Accessed: 2019-11-28.
URL: <https://github.com/barche/MPIArrays.jl>
- Jia, Y., Shelhamer, E., Donahue, J., Karayev, S., Long, J., Girshick, R., Guadarrama, S. and Darrell, T. (2014), Caffe: Convolutional architecture for fast feature embedding, *in* ‘Proceedings of the 22nd ACM international conference on Multimedia’, ACM, pp. 675–678.
- Jordan, M. I., Lee, J. D. and Yang, Y. (2019), ‘Communication-efficient distributed statistical inference’, *Journal of the American Statistical Association* **114**(526), 668–681.
- JuliaParallel Team (n.d.), ‘DistributedArrays.jl: Distributed arrays in Julia’. Accessed: 2019-11-28.
URL: <https://github.com/JuliaParallel/DistributedArrays.jl>
- Keys, K. L., Zhou, H. and Lange, K. (2019), ‘Proximal distance algorithms: Theory and practice.’, *Journal of Machine Learning Research* **20**(66), 1–38.
- Klößner, A., Pinto, N., Lee, Y., Catanzaro, B., Ivanov, P. and Fasih, A. (2012), ‘PyCUDA and PyOpenCL: A scripting-based approach to GPU run-time code generation’, *Parallel Computing* **38**(3), 157–174.
- Ko, S. and Won, J.-H. (2019), Optimal minimization of the sum of three convex functions with a linear operator, *in* ‘The 22nd International Conference on Artificial Intelligence and Statistics’, pp. 1185–1194.
- Ko, S., Yu, D. and Won, J.-H. (2019+), ‘Easily parallelizable and distributable class of algorithms for structured sparsity, with optimal acceleration’, *Journal of Computational and Graphical Statistics* (to appear).
- Koanantakool, P., Ali, A., Azad, A., Buluc, A., Morozov, D., Olikier, L., Yelick, K. and Oh, S.-Y. (2018), Communication-avoiding optimization methods for distributed massive-scale sparse inverse covariance estimation, *in* ‘International Conference on Artificial Intelligence and Statistics’, pp. 1376–1386.
- Koanantakool, P., Azad, A., Buluç, A., Morozov, D., Oh, S.-Y., Olikier, L. and Yelick, K. (2016), Communication-avoiding parallel sparse-dense matrix-matrix multiplication, *in* ‘2016 IEEE International Parallel and Distributed Processing Symposium (IPDPS)’, IEEE, pp. 842–853.
- Lam, S. K., Pitrou, A. and Seibert, S. (2015), Numba: A LLVM-based Python JIT compiler, *in* ‘Proceedings of the Second Workshop on the LLVM Compiler Infrastructure in HPC’, ACM, p. 7.
- Lange, K. (2016), *MM Optimization Algorithms*, Vol. 147, SIAM.
- Lange, K. and Carson, R. (1984), ‘EM reconstruction algorithms for emission and transmission tomography’, *Journal of Computer Assisted Tomography* **8**(2), 306–16.
- Lange, K., Hunter, D. R. and Yang, I. (2000), ‘Optimization transfer using surrogate objective functions’, *Journal of Computational and Graphical Statistics* **9**(1), 1–20.
- LeCun, Y., Bengio, Y. and Hinton, G. (2015), ‘Deep learning’, *Nature* **521**(7553), 436.
- Lee, D. D. and Seung, H. S. (1999), ‘Learning the parts of objects by non-negative matrix factorization’, *Nature* **401**(6755), 788.
- Lee, D. D. and Seung, H. S. (2001), Algorithms for non-negative matrix factorization, *in* ‘Advances in neural information processing systems’, pp. 556–562.
- Lee, T., Won, J.-H., Lim, J. and Yoon, S. (2017), ‘Large-scale structured sparsity via parallel fused lasso on multiple GPUs’, *Journal of Computational and Graphical Statistics*

- 26(4), 851–864.
- Li, Q., Kecman, V. and Salman, R. (2010), A chunking method for Euclidean distance matrix calculation on large dataset using multi-GPU, *in* ‘2010 Ninth International Conference on Machine Learning and Applications’, IEEE, pp. 208–213.
- Lim, H., Dewaraja, Y. K. and Fessler, J. A. (2018), ‘A PET reconstruction formulation that enforces non-negativity in projection space for bias reduction in Y-90 imaging’, *Physics in Medicine & Biology* **63**(3), 035042.
- Lin, C.-J. (2007), ‘Projected gradient methods for nonnegative matrix factorization’, *Neural Computation* **19**(10), 2756–2779.
- Liu, C., Yang, H.-c., Fan, J., He, L.-W. and Wang, Y.-M. (2010), Distributed nonnegative matrix factorization for web-scale dyadic data analysis on MapReduce, *in* ‘Proceedings of the 19th International Conference on World Wide Web’, ACM, pp. 681–690.
- Mahajan, A., Taliun, D., Thurner, M., Robertson, N. R., Torres, J. M., Rayner, N. W., Payne, A. J., Steinhorsdottir, V., Scott, R. A., Grarup, N. et al. (2018), ‘Fine-mapping type 2 diabetes loci to single-variant resolution using high-density imputation and islet-specific epigenome maps’, *Nature Genetics* **50**(11), 1505.
- McLaren, W., Gil, L., Hunt, S. E., Riat, H. S., Ritchie, G. R., Thormann, A., Flicek, P. and Cunningham, F. (2016), ‘The Ensembl variant effect predictor’, *Genome Biology* **17**(1), 122.
- Mittal, S., Madigan, D., Burd, R. S. and Suchard, M. A. (2014), ‘High-dimensional, massive sample-size Cox proportional hazards regression for survival analysis’, *Biostatistics* **15**(2), 207–221.
- Munshi, A. (2009), The OpenCL specification, *in* ‘2009 IEEE Hot Chips 21 Symposium (HCS)’, IEEE, pp. 1–314.
- Nakano, J. (2012), Parallel computing techniques, *in* ‘Handbook of Computational Statistics’, Springer, pp. 243–271.
- Negahban, S. N., Ravikumar, P., Wainwright, M. J. and Yu, B. (2012), ‘A unified framework for high-dimensional analysis of M -estimators with decomposable regularizers’, *Statistical Science* **27**(4), 538–557.
- NERSC (n.d.), ‘Distributed TensorFlow’. Accessed: 2019-12-03.
URL: <https://docs.nersc.gov/analytics/machinelearning/tensorflow/#distributed-tensorflow>
- Ng, M. C., Shriner, D., Chen, B. H., Li, J., Chen, W.-M., Guo, X., Liu, J., Bielinski, S. J., Yanek, L. R., Nalls, M. A. et al. (2014), ‘Meta-analysis of genome-wide association studies in african americans provides insights into the genetic architecture of type 2 diabetes’, *PLoS Genetics* **10**(8), e1004517.
- Nvidia (2007), ‘Nvidia CUDA compute unified device architecture programming guide, Version 1.0’.
- NVIDIA (2013), ‘Basic linear algebra subroutines (cuBLAS) library’. Accessed: 2019-11-28.
URL: <http://docs.nvidia.com/cuda/cublas>
- NVIDIA (2018), ‘Sparse matrix library (cuSPARSE)’. Accessed: 2019-11-28.
URL: <http://docs.nvidia.com/cuda/cuspars>
- Owens, J. D., Luebke, D., Govindaraju, N., Harris, M., Krüger, J., Lefohn, A. E. and Purcell, T. J. (2007), A survey of general-purpose computation on graphics hardware, *in* ‘Computer Graphics Forum’, Vol. 26, Wiley Online Library, pp. 80–113.
- Parikh, N. and Boyd, S. (2014), ‘Proximal algorithms’, *Foundations and Trends in Optimization* **1**(3), 127–239.
- Paszke, A., Gross, S., Chintala, S., Chanan, G., Yang, E., DeVito, Z., Lin, Z., Desmaison, A., Antiga, L. and Lerer, A. (2017), Automatic differentiation in PyTorch, *in* ‘NIPS Autodiff Workshop’.

URL: <http://pytorch.org>

- Polson, N. G., Scott, J. G. and Willard, B. T. (2015), ‘Proximal algorithms in statistics and machine learning’, *Statistical Science* **30**(4), 559–581.
- R Core Team (2018), *R: A Language and Environment for Statistical Computing*, R Foundation for Statistical Computing, Vienna, Austria. Accessed: 2019-11-28.
- URL:** <https://www.R-project.org/>
- Raina, R., Madhavan, A. and Ng, A. Y. (2009), Large-scale deep unsupervised learning using graphics processors, in ‘Proceedings of the 26th Annual International Conference on Machine Learning’, ACM, pp. 873–880.
- Ramdas, A. and Tibshirani, R. J. (2016), ‘Fast and flexible ADMM algorithms for trend filtering’, *Journal of Computational and Graphical Statistics* **25**(3), 839–858.
- Roland, C., Varadhan, R. and Frangakis, C. (2007), ‘Squared polynomial extrapolation methods with cycling: an application to the positron emission tomography problem’, *Numerical Algorithms* **44**(2), 159–172.
- RStudio (n.d.), ‘tensorflow: R interface to TensorFlow’. Accessed: 2019-11-28.
- URL:** <https://tensorflow.rstudio.com/>
- Rudin, L. I., Osher, S. and Fatemi, E. (1992), ‘Nonlinear total variation based noise removal algorithms’, *Physica D: Nonlinear Phenomena* **60**(1), 259–268.
- Rumelhart, D. E., Hinton, G. E. and Williams, R. J. (1988), ‘Learning representations by back-propagating errors’, *Cognitive Modeling* **5**(3), 1.
- Ryu, E. K., Ko, S. and Won, J.-H. (2019+), ‘Splitting with near-circulant linear systems: applications to total variation CT and PET’, *SIAM Journal on Scientific Computing* (to appear).
- Scott, L. J., Mohlke, K. L., Bonnycastle, L. L., Willer, C. J., Li, Y., Duren, W. L., Erdos, M. R., Stringham, H. M., Chines, P. S., Jackson, A. U. et al. (2007), ‘A genome-wide association study of type 2 diabetes in finns detects multiple susceptibility variants’, *Science* **316**(5829), 1341–1345.
- Seide, F. and Agarwal, A. (2016), CNTK: Microsoft’s open-source deep-learning toolkit, in ‘Proceedings of the 22nd ACM SIGKDD International Conference on Knowledge Discovery and Data Mining’, ACM, pp. 2135–2135.
- Sergeev, A. and Del Balso, M. (2018), ‘Horovod: fast and easy distributed deep learning in tensorflow’, *arXiv preprint arXiv:1802.05799*.
- Solo.io (n.d.), ‘Gloo: an Envoy-powered API gateway’. Accessed: 2019-11-28.
- URL:** <https://docs.solo.io/gloo/latest/>
- Staples, G. (2006), Torque resource manager, in ‘Proceedings of the 2006 ACM/IEEE conference on Supercomputing’, ACM, p. 8.
- Suchard, M. A., Holmes, C. and West, M. (2010), ‘Some of the what?, why?, how?, who? and where? of graphics processing unit computing for Bayesian analysis’, *Bulletin of the International Society for Bayesian Analysis* **17**(1), 12–16.
- Suchard, M. A., Simpson, S. E., Zorych, I., Ryan, P. and Madigan, D. (2013), ‘Massive parallelization of serial inference algorithms for a complex generalized linear model’, *ACM Transactions on Modeling and Computer Simulation* **23**(1), 10.
- Suchard, M. A., Wang, Q., Chan, C., Frelinger, J., Cron, A. and West, M. (2010), ‘Understanding GPU programming for statistical computation: Studies in massively parallel massive mixtures’, *Journal of Computational and Graphical Statistics* **19**(2), 419–438.
- Sudlow, C., Gallacher, J., Allen, N., Beral, V., Burton, P., Danesh, J., Downey, P., Elliott, P., Green, J., Landray, M. et al. (2015), ‘UK Biobank: an open access resource for identifying the causes of a wide range of complex diseases of middle and old age’, *PLoS Medicine* **12**(3), e1001779.
- The Wellcome Trust Case Control Consortium (2007), ‘Genome-wide association study of

- 14,000 cases of seven common diseases and 3,000 shared controls’, *Nature* **447**(7145), 661.
- Tibshirani, R. (1996), ‘Regression shrinkage and selection via the lasso’, *Journal of the Royal Statistical Society: Series B (Methodological)* **58**(1), 267–288.
- Tibshirani, R. J. and Taylor, J. (2011), ‘The solution path of the generalized lasso’, *The Annals of Statistics* **39**(3), 1335–1371.
- Tieleman, T. (2010), ‘Gnumpy: an easy way to use GPU boards in Python’, *Department of Computer Science, University of Toronto*.
- University of Zurich (n.d.), ‘ElastiCluster’. Accessed: 2019-12-06.
URL: <https://elasticcluster.readthedocs.io/en/latest/>
- Ushey, K., Allaire, J. and Tang, Y. (2019), *reticulate: Interface to ‘Python’*. R package version 1.13, Accessed: 2019-11-28.
URL: <https://CRAN.R-project.org/package=reticulate>
- Van De Geijn, R. A. and Watts, J. (1997), ‘SUMMA: Scalable universal matrix multiplication algorithm’, *Concurrency: Practice and Experience* **9**(4), 255–274.
- van Rossum, G. (1995), ‘Python tutorial, technical report cs-r9526’, *Centrum voor Wiskunde en Informatica (CWI), Amsterdam*.
- Vardi, Y., Shepp, L. A. and Kaufman, L. (1985), ‘A statistical model for positron emission tomography’, *Journal of the American Statistical Association* **80**(389), 8–20.
- Voight, B. F., Scott, L. J., Steinthorsdottir, V., Morris, A. P., Dina, C., Welch, R. P., Zeggini, E., Huth, C., Aulchenko, Y. S., Thorleifsson, G. et al. (2010), ‘Twelve type 2 diabetes susceptibility loci identified through large-scale association analysis’, *Nature Genetics* **42**(7), 579.
- Vũ, B. C. (2013), ‘A splitting algorithm for dual monotone inclusions involving cocoercive operators’, *Advances in Computational Mathematics* **38**(3), 667–681.
- Walker, E. (2008), ‘Benchmarking Amazon EC2 for high-performance scientific computing’, *login: the Magazine of USENIX & SAGE* **33**(5), 18–23.
- Wang, E., Zhang, Q., Shen, B., Zhang, G., Lu, X., Wu, Q. and Wang, Y. (2014), Intel math kernel library, in ‘High-Performance Computing on the Intel® Xeon Phi’, Springer, pp. 167–188.
- Wang, Y.-X. and Zhang, Y.-J. (2013), ‘Nonnegative matrix factorization: A comprehensive review’, *IEEE Transactions on Knowledge and Data Engineering* **25**(6), 1336–1353.
- Whitehead, N. and Fit-Florea, A. (2011), ‘Precision & performance: Floating point and IEEE 754 compliance for NVIDIA GPUs’, *Technical Report, Nvidia Corporation*.
- Wu, T. T. and Lange, K. (2010), ‘The MM alternative to EM’, *Statistical Science* **25**(4), 492–505.
- Xianyi, Z., Qian, W. and Chothia, Z. (2014), ‘OpenBLAS: An optimized BLAS library’. Accessed: 2019-11-28.
URL: <https://www.openblas.net/>
- Xue, L., Ma, S. and Zou, H. (2012), ‘Positive-definite ℓ_1 -penalized estimation of large covariance matrices’, *Journal of the American Statistical Association* **107**(500), 1480–1491.
- Yoo, A. B., Jette, M. A. and Grondona, M. (2003), Slurm: Simple linux utility for resource management, in ‘Workshop on Job Scheduling Strategies for Parallel Processing’, Springer, pp. 44–60.
- Yu, D., Won, J.-H., Lee, T., Lim, J. and Yoon, S. (2015), ‘High-dimensional fused lasso regression using majorization–minimization and parallel processing’, *Journal of Computational and Graphical Statistics* **24**(1), 121–153.
- Zhou, H., Lange, K. and Suchard, M. A. (2010), ‘Graphics processing units and high-dimensional optimization’, *Statistical Science* **25**(3), 311.
- Zhu, M. and Chan, T. (2008), ‘An efficient primal-dual hybrid gradient algorithm for total variation image restoration’, *UCLA CAM Report* (08-34).

Zhu, Y. (2017), ‘An augmented ADMM algorithm with application to the generalized lasso problem’, *Journal of Computational and Graphical Statistics* **26**(1), 195–204.

Appendix A: A brief introduction to PyTorch

In this section, we introduce simple operations on PyTorch. Note that Python uses 0-based, row-major ordering, like C and C++ (R is 1-based, column-major ordering). First we import the PyTorch library. This is equivalent to `library()` in R.

```
import torch
```

Tensor creation

The following is equivalent to `set.seed()` in R.

```
torch.manual_seed(100)
```

One may create an uninitialized tensor. This creates a 3×4 tensor (matrix).

```
torch.empty(3, 4) # uninitialized tensor

tensor([[ -393462160144990208.0000,          0.0000,
          -393462160144990208.0000,          0.0000],
        [          0.0000,          0.0000,
          0.0000,          0.0000],
        [          0.0000,          0.0000,
          0.0000,          0.0000]])
```

This generates a tensor initialized with random values from $(0, 1)$.

```
y = torch.rand(3, 4) # from Unif(0, 1)

tensor([[0.1117, 0.8158, 0.2626, 0.4839],
        [0.6765, 0.7539, 0.2627, 0.0428],
        [0.2080, 0.1180, 0.1217, 0.7356]])
```

We can also generate a tensor filled with zeros or ones.

```
z = torch.ones(3, 4) # torch.zeros(3, 4)

tensor([[1., 1., 1., 1.],
        [1., 1., 1., 1.],
        [1., 1., 1., 1.]])
```

A tensor can be created from standard Python data.

```
w = torch.tensor([3, 4, 5, 6])

tensor([3, 4, 5, 6])
```

Indexing

The following are standard method of indexing tensors.

```
y[2, 3] # indexing: zero-based, returns a 0-dimensional tensor
```

```
tensor(0.7356)
```

The indexing always returns a (sub)tensor, even for scalars (treated as zero-dimensional tensors). A standard Python number can be returned by using `.item()`.

```
y[2, 3].item() # A standard Python floating-point number
```

```
0.7355988621711731
```

To get a column from a tensor, we use the indexing as below. The syntax is similar but slightly different from R.

```
y[:, 3] # 3rd column. The leftmost column is 0th. cf. y[, 4] in R
```

```
tensor([0.4839, 0.0428, 0.7356])
```

The following is for taking a row.

```
y[2, :] # 2nd row. The top row is 0th. cf. y[3, ] in R
```

```
tensor([0.2080, 0.1180, 0.1217, 0.7356])
```

Simple operations

Here we provide an example of simple operations on PyTorch. Addition using the operator `+` acts just like anyone can expect:

```
x = y + z # a simple addition.
```

```
tensor([[1.1117, 1.8158, 1.2626, 1.4839],
        [1.6765, 1.7539, 1.2627, 1.0428],
        [1.2080, 1.1180, 1.1217, 1.7356]])
```

Here is another form of addition.

```
x = torch.add(y, z) # another syntax for addition
```

The operators ending with an underscore (`_`) changes the value of the tensor in-place.

```
y.add_(z) # in-place addition
```

```
tensor([[1.1117, 1.8158, 1.2626, 1.4839],
        [1.6765, 1.7539, 1.2627, 1.0428],
        [1.2080, 1.1180, 1.1217, 1.7356]])
```

Concatenation

We can concatenate the tensors using the function `cat()`, which resembles `c()`, `cbind()`, and `rbind()` in R. The second argument indicates the dimension that the tensors are concatenated along: zero means by concatenation rows, and one means by columns.

```
torch.cat((y, z), 0) # along the rows
```

```

tensor([[1.1117, 1.8158, 1.2626, 1.4839],
        [1.6765, 1.7539, 1.2627, 1.0428],
        [1.2080, 1.1180, 1.1217, 1.7356],
        [1.0000, 1.0000, 1.0000, 1.0000],
        [1.0000, 1.0000, 1.0000, 1.0000],
        [1.0000, 1.0000, 1.0000, 1.0000]])

torch.cat((y, z), 1) # along the columns

tensor([[1.1117, 1.8158, 1.2626, 1.4839, 1.0000, 1.0000, 1.0000, 1.0000],
        [1.6765, 1.7539, 1.2627, 1.0428, 1.0000, 1.0000, 1.0000, 1.0000],
        [1.2080, 1.1180, 1.1217, 1.7356, 1.0000, 1.0000, 1.0000, 1.0000]])

```

Reshaping

One can reshape a tensor, like changing the attribute dim in R.

```

y.view(12) # 1-dimensional array

tensor([1.1117, 1.8158, 1.2626, 1.4839, 1.6765, 1.7539, 1.2627, 1.0428, 1.2080,
        1.1180, 1.1217, 1.7356])

```

Up to one of the arguments of `view()` can be `-1`. The size of the reshaped tensor is inferred from the other dimensions.

```

# reshape into (6)-by-2 tensor;
# (6) is inferred from the other dimension
y.view(-1, 2)

tensor([[1.1117, 1.8158],
        [1.2626, 1.4839],
        [1.6765, 1.7539],
        [1.2627, 1.0428],
        [1.2080, 1.1180],
        [1.1217, 1.7356]])

```

Appendix B: Monte Carlo estimation of π on multi-GPU using TensorFlow

This section shows an implementation of Monte Carlo estimation example in Section 3.2 in multi-GPU using TensorFlow. Listing B.1 is the implementation that assumes a node with four GPUs. The code appears more or less the same as Listing 1, except that the list of devices is pre-specified. Line 2 indicates that a static computational graph is used (instead of the eager execution) for the function to run simultaneously on multiple GPUs. It is slightly shorter than Listing 1, partially because multi-GPU is supported natively in TensorFlow, and MPI is not used.

Appendix C: AWS EC2 and ParallelCluster

We used AWS Elastic Compute Cloud (EC2) via CfnCluster throughout our multi CPU-node experiments, which is updated to ParallelCluster after we had completed the experiments. In this section, we instruct how to use ParallelCluster via Amazon Web Services. This section is structured into three parts: setting up AWS account and how to configure and run a job on ParallelCluster. We refer the readers to the official documentation¹ and an AWS whitepaper² for further details.

¹<https://docs.aws.amazon.com/parallelcluster/index.html>

²https://dl.awsstatic.com/Projects/P4114756/deploy-elastic-hpc-cluster_project.a12a8c61339522e21262da10a6b43a3678099220.pdf

```

1 import tensorflow as tf
2
3 # Enforce graph computation. With eager execution, the code runs
4 # sequentially w.r.t. GPUs. e.g., computation for '/gpu:1' would not
5 # start until the computation for '/gpu:0' finishes.
6 @tf.function
7 def mc_pi(n, devices):
8     estim = []
9     for d in devices:
10        # use device d in this block
11        with tf.device(d):
12            x = tf.random.uniform((n,), dtype=tf.float64)
13            y = tf.random.uniform((n,), dtype=tf.float64)
14            # compute local estimate of pi
15            # and save it as an element of 'estim'.
16            estim.append(tf.reduce_mean(tf.cast(x ** 2 +
17            y ** 2 < 1, tf.float64)) * 4)
18    return tf.add_n(estim)/len(devices)
19
20 if __name__ == '__main__':
21    n = 10000
22    devices = ['/gpu:0', '/gpu:1', '/gpu:2', '/gpu:3']
23    r = mc_pi(n, devices)
24    print(r.numpy())

```

Listing B.1: Monte Carlo estimation of π for TensorFlow on a workstation with multiple GPUs

C.1. Overview

A virtual cluster created by ParallelCluster consists of two types of *instances* in EC2: a *master* node and multiple *worker* instances. The master instance manages *jobs* through a queue on a *job scheduler* and several AWS services such as *Simple Queue Service* and *Auto Scaling Group*. When a virtual cluster is created, the *shared file system*. The software necessary for the jobs are installed in this file system, and a script to set up the environment variables for the tools is utilized. While the master instance does not directly take part in the actual computation, the speed of network on the shared file system depends on the instance type of the master instance. If the jobs depend on the shared dataset, the master instance has to allow fast enough network speed. The actual computation is performed on the worker instances. Each worker has access to the shared file system where the necessary tools and data reside. The network speed between workers depends on the worker instance type.

C.2. Glossary

We briefly introduce some of the key concepts regarding the AWS and cluster computing in this subsection.

Some of the basic concepts from AWS are shown below:

- Instance: a virtual computer on AWS EC2. There are various types of instances determines number of cores, memory size, network speed, etc. `c5.18xlarge` is prominently utilized in our experiments.³

³See <https://aws.amazon.com/en/ec2/instance-types/> for the full list of types of instances.

- Region: a region, e.g., North Virginia, Ohio, North California, Oregon, Hong Kong, Seoul, Tokyo is completely independent from other regions, and data transfer between regions are charged.
- Availability zone: there are a handful of availability zones in each region. Each availability zone is isolated, but availability zones in the same region is interconnected with a low-latency network. Note that a virtual cluster created by ParallelCluster is tied to a single availability zone.

Listed below are some, but not all, of the AWS services involved in ParallelCluster. They are all managed automatically through ParallelCluster and can be modified through the AWS console.

- Elastic Compute Cloud (EC2): the core service of AWS that allows users to rent virtual computers. There are three methods of payment available:
 - On-demand: hourly charged, without risk of interruption.
 - Spot: bid-based charging. Serviced at up to 70%-discounted rate, but is interrupted if the price goes higher than the bid price.
 - Reserved: one-time payment at discounted rate.
- Elastic Block Store (EBS): persistent block storage volume for EC2 instances, e.g. a solid-state drive (SSD). In ParallelCluster, each instance is started with a root EBS volume exclusive to each instance.
- CloudFormation: An interface that describes and provisions the cloud resources.
- Simple Queue Service: the actual job queue is served through message passing between EC2 instances.
- CloudWatch: monitors and manages the cloud.
- Auto Scaling Group: a collection of EC2 instances with similar characteristics. The number of instances is automatically scaled based on criteria defined over CloudWatch.
- Identity and Access Management (IAM): An IAM user is an “entity that [one] creates in AWS to represent the person or application that uses it to interact with AWS.”⁴ Each IAM user is granted certain permissions determined by the root user. As there are many services involved in ParallelCluster, it is recommended to use an IAM user with full permission.
- Virtual Private Cloud (VPC): a VPC is a dedicated virtual network exclusive to the user, isolated from any other VPCs, which spans all the availability zones in one region. A subnet is a subnetwork in VPC exclusive to a single availability zone.⁵
- Security Group (SG): A security group acts as a “virtual firewall that controls the traffic for one or more instances.”⁶

Here are some of the concepts related to cluster computing:

- Shared file system: for multiple instances to work on the same data, it is convenient to have a file system that can be accessed by all the instances involved. In ParallelCluster, it is implemented as an additional EBS volume attached to the master instance. All the worker instances can access this volume, and its speed of network depends on the instance type of the master instance.
- Job: a unit of execution. defined by either a single command or a job script.
- Queue: a data structure containing jobs to run. Jobs in a queue is managed and prioritized by a job scheduler.
- Master: an instance that manages the job scheduler.
- Worker: an instance that executes the jobs.
- Job scheduler: an application program that controls the execution of jobs over a cluster. e.g. Sun Grid Engine, Torque, Slurm, etc. The Sun Grid Engine (SGE) was used for our experiments.

Several SGE commands are as follows:

⁴https://docs.aws.amazon.com/IAM/latest/UserGuide/id_users.html

⁵https://docs.aws.amazon.com/vpc/latest/userguide/VPC_Subnets.html

⁶<https://docs.aws.amazon.com/AWSEC2/latest/UserGuide/using-network-security.html>

- `qsub`: submits a job to the job queue
- `qdel`: removes a job on the job queue
- `qstat`: shows the current status of the queue
- `qhost`: shows the current list of workers

C.3. Prerequisites

The following are needed before we proceed. Most of these might be considered the first steps to use AWS.

- Access keys with administrative privileges: Access keys are credentials for IAM users and root users. They consist of access key ID (analogous to username) and secret access key (analogous to passwords). They should be kept confidential. It is recommended to create a temporary IAM user with administrative privilege and create an access key ID and a secret access key for the IAM user. They can be created in the AWS console (or the IAM console for an IAM user).⁷
- A VPC and a subnet: A VPC for each region and a subnet for each availability zone is created by default. One may use these default VPC and subnet or newly-created ones.
- A security group: One may use a default security group or a newly-created one.
- A key pair that allows the user to access the cloud via SSH: Amazon EC2 uses public-key cryptography for login credentials. Each EC2 instance is configured with a public key, and the user has to access this instance using the matching private key. It can be generated and managed on AWS EC2 console as well as the user's terminal.⁸

C.4. Installation

First, we install the ParallelCluster command line interface (CLI) on a local machine. ParallelCluster command line interface is distributed through the standard Python Package Index (PyPI), so one may install it through `pip`, the standard package-installing command for Python. One may install ParallelCluster by executing the following on the command line:

```
sudo pip install aws-parallelcluster
```

C.5. Configuration

Once ParallelCluster is installed on a local machine, an initial configuration is needed. It can be done by various ways, but the easiest way is through the command below:

```
pcluster configure
```

Then, the interactive dialog to setup ParallelCluster appears:

```
ParallelCluster Template [default]: <a name desired>
AWS Access Key ID []: <copy and paste the access key>
AWS Secret Access Key ID []: <copy and paste the secret key>
Acceptable Values for AWS Region ID:
  eu-north-1
  ap-south-1
  eu-west-3
  eu-west-2
```

⁷https://docs.aws.amazon.com/IAM/latest/UserGuide/id_credentials_access-keys.html

⁸<https://docs.aws.amazon.com/AWSEC2/latest/UserGuide/ec2-key-pairs.html>

```

eu-west-1
ap-northeast-2
ap-northeast-1
sa-east-1
ca-central-1
ap-southeast-1
ap-southeast-2
eu-central-1
us-east-1
us-east-2
us-west-1
us-west-2
AWS Region ID [ap-northeast-2]: <the region to use>
VPC Name [<default name>]: <a name desired>
Acceptable Values for Key Name:
    <the registered key names appear here>
Key Name []: <enter the EC2 key pair name>
Acceptable Values for VPC ID:
    <the list of VPC appears here>
VPC ID []: <enter one of the vpc above>
Acceptable Values for Master Subnet ID:
    <the list of subnet ids appears here>
Master Subnet ID [subnet-<default value>]: <enter one of the master subnet id above>

```

Now examine the files in the directory `~/.parallelcluster` (a hidden directory under the home directory). The file `pcluster-cli.log` shows the log and the file `config` shows the configuration. One can modify the file `config` to fine-tune the configuration per user's need. The following is the config corresponding to our CfnCluster experiments:

```

[global]
update_check = true
sanity_check = true
cluster_template = test

[aws]
aws_region_name = ap-northeast-2

[cluster test]
vpc_settings = testcfn
key_name = <key name>
initial_queue_size = 0
max_queue_size = 20
ebs_settings = expr_ebs
scheduler = sge
compute_instance_type = c5.18xlarge
master_instance_type = c5.18xlarge
cluster_type = spot
spot_price = 1.20
base_os = centos7
scaling_settings = custom
extra_json = {"cluster" : { "cfn_scheduler_slots" : "2" } }
master_root_volume_size = 20
compute_root_volume_size = 20

[ebs expr_ebs]

```

```

ebs_snapshot_id = < a snapshot id >
volume_size = 40

[vpc testcfn]
master_subnet_id = < a subnet id >
vpc_id = < a vpc id >

[aliases]
ssh = ssh {CFN_USER}@{MASTER_IP} {ARGS}

[scaling custom]
scaling_idletime = 20

```

In the `[global]` section, we set global configurations. The `cluster_template` names the cluster section to be used for the cluster.

`update_check` check for the updates to `ParallelCluster`, and `sanity_check` validates that resources defined in parameters.

In the `[aws]` section, the region is specified. AWS access key and secret key may appear here unless specified in the base AWS CLI.

In the `[cluster]` section, we define the detailed specification of the virtual cluster. The `vpc_settings` names a setting for VPC, detailed in the `[vpc]` section, and the `ebs_settings` names the setting for EBS, detailed in `[ebs]` section. The `key_name` defines the key name to use. The `initial_queue_size` defines the number of worker instances at the launch of the cluster. We used zero for our experiments, as we often needed to check if the configuration is done properly on master before running actual jobs. The worker instances are launched upon submission of a new job into the queue, and they are terminated when the workers stay idle for a while (not exactly defined, but often around five to ten minutes).

We set the `max_queue_size`, the maximum number of worker instances to 20. We used CentOS 7 as the `base_os` for our instances. The `master_root_volume_size` and the `compute_root_volume_size` determine the size of root volume of the master instance and each of the worker instance, respectively. For the scheduler, we used the Sun Grid Engine (`sge`). For the `compute_instance_type`, we used `c5.18xlarge`, an instance with 36 physical cores (72 virtual cores with hyperthreading). It consists of two non-uniform memory access (NUMA) nodes with 18 physical cores each. In NUMA memory design, an access to local memory of a processor is faster than an access to non-local memory within a shared memory system. `master_instance_type` defines the instance type of the master. Sometimes it is fine to be as small as `t2.micro`, a single-core instance, but we needed an instance with good network performance when many instances simultaneously accessed a large data file on shared storage. The `cluster_type` is either `ondemand` (default) or `spot`. For `c5.18xlarge` in Seoul region (`ap-northeast-2`), on-demand price was \$3.456 per instance-hour, while the spot price was at \$1.0788 per instance-hour throughout the duration of our experiments. Budget-constrained users may use spot instances for worker instances. In case of this scenario, the `spot_prices` was set to \$1.20 per instance-hour, so if the actual price went above this value, our worker instances would have been terminated. Only the on-demand instance could be used as the master instance, so smaller instance might be desirable for lower cost. The setting `extra_json = {"cluster" : { "cfn_scheduler_slots" : "2" } }` sets number of slots that an instance bears to two. Each computing job is required to declare the number of “slots” to occupy. By default, the number of slots per instance is the number of virtual cores the instance has. This default setting is natural, but a problem arises if we intend to utilize shared-memory parallelism in NUMA node-level, as the number of slots occupied is tied to the number of instances launched. We assigned one slot per NUMA node that an instance has (i.e., 2 slots per instance), and utilized all 18 physical cores per NUMA node.

The `[ebs]` section defines the configuration for the EBS volume mounted on the master node and shared via NFS to workers. The `ebs_snapshot_id` defines the ID of the EBS snapshot to be used. We had datasets and packages necessary for our jobs pre-installed in an EBS volume and created a snapshot. The size of the volume was 40 GB. By default, the volume is mounted to the

path /shared.

We refer the readers to <https://docs.aws.amazon.com/parallelcluster/> for further details.

C.6. Creating, accessing, and destroying the cluster

We can create a virtual cluster named `example` by issuing the following command on a local machine:

```
pcluster create example
```

To access the master instance through ssh, one needs the location of the private key (`.pem`) file. The command to use is:

```
pcluster ssh example -i <private key file>
```

The default username for instances with CentOS is `centos`. The default username depends on the Amazon Machine Image (AMI) being used to create a virtual machine, which is determined by the `base_os` selected on the configuration. The names of the existing clusters can be listed using the command `pcluster list`, and we may completely remove a cluster `example` using the command `pcluster delete example`.

C.7. Installation of libraries

Now we can access the master node through secure shell (SSH). We have a shared EBS volume mounted at `/shared`, and we are to install necessary software there. For our experiments, we installed `anaconda`, a portable installation of Python, in the directory `/shared`. A script to set up environment variables is also created and saved in `/shared`:

```
# setup.sh
module load mpi/openmpi-x86_64 # loads MPI to the environment
source /shared/conda/etc/profile.d/conda.sh
export PATH=/shared/conda/bin:$PATH
export LD_LIBRARY_PATH=/shared/conda/lib:$LD_LIBRARY_PATH
```

We issued the command:

```
source setup.sh
```

to set up the environment variables. We installed PyTorch from source⁹, as it is required to do so in order to incorporate MPI.

To download our code, one can issue the command:

```
git clone https://github.com/kose-y/dist_stat /shared/dist_stat
```

C.8. Running a job

To provide instructions on how to define the environment to each instance, we need a script defining each job. The following script `mcpic-2.job` is for running the program for Monte Carlo estimation of π in Section 3 (Listing 1) using two instances (four processes using 18 threads each).

⁹<https://github.com/pytorch/pytorch#from-source>

```
#!/bin/sh
#$ -cwd
#$ -N mcpi
#$ -pe mpi 4
#$ -j y
date
source /shared/conda/etc/profile.d/conda.sh
export PATH=/shared/conda/bin:$PATH
export LD_LIBRARY_PATH=/shared/conda/lib:$LD_LIBRARY_PATH
export MKL_NUM_THREADS=18
mpirun -np 4 python /shared/dist_stat/examples/mcpi-mpi-pytorch.py
```

The line `-pe mpi 4` tells the scheduler that we are using four slots. Setting the value of the environment variable `MKL_NUM_THREADS` to 18 means that MKL runs with 18 threads or cores for that process. We launch four processes in the cluster, two per instance, as defined by our `ParallelCluster` setup, in parallel using MPI. We can submit this job to the Sun Grid Engine (the job scheduler) using the command:

```
qsub mcpi-2.job
```

When we submit a job, a message similar to the following appears:

```
Your job 130 ("mcpi") has been submitted
```

One may see the newly submitted job in the queue using the command `qstat`.

```
qstat
```

job-ID	prior	name	user	state	submit/start at	queue	slots	ja-task-ID
130	0.55500	mcpi	centos	qw	02/28/2019 03:58:54		4	

If we want to delete any job waiting for the queue or running, use the command `qdel`.

```
qdel 130
```

```
centos has deleted job 130
```

Once the job is completed, the output is saved as a text file named such as `mcpi.o130`. For example:

```
Thu Feb 28 04:07:54 UTC 2019
3.148
```

The scripts for our numerical examples are in `/shared/dist_stat/jobs`.

C.9. Miscellaneous

To keep what is on the EBS volume on the cloud and access later, we need to create a snapshot for the volume. We can later create a volume based on this snapshot¹⁰, and mount it on any instance¹¹. In `ParallelCluster`, this is done automatically when we give an ID of a snapshot in the `config` file.

¹⁰<https://docs.aws.amazon.com/AWSEC2/latest/UserGuide/ebs-creating-snapshot.html>

¹¹<https://docs.aws.amazon.com/AWSEC2/latest/UserGuide/ebs-using-volumes.html>

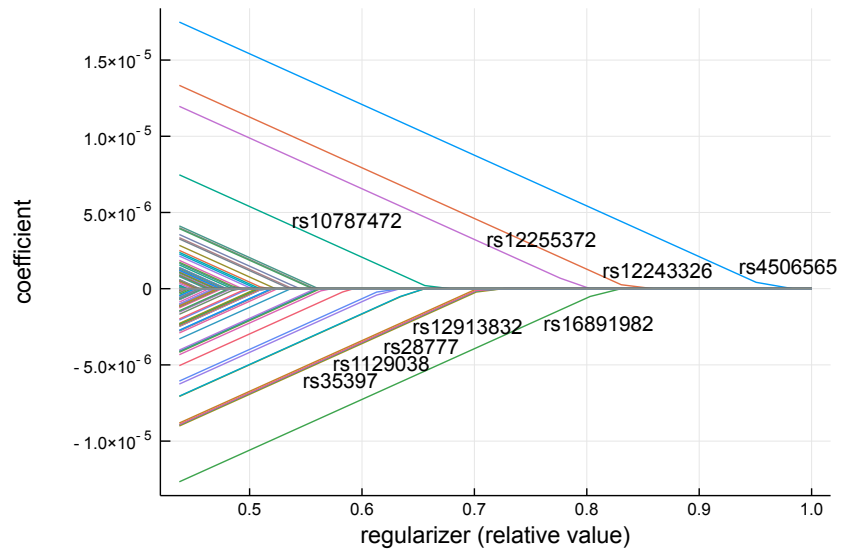


Fig D.1: Solution path for ℓ_1 -regularized Cox regression on the UK Biobank dataset. Signs are with respect to the reference allele: positive value favors alternative allele as the risk allele.

Appendix D: Details of SNPs selected in ℓ_1 -regularized Cox regression

Figure D.1 shows the solution path for SNPs within the range we used for the experiment in Section 6.5. Tables D.1 and D.2 list the 111 selected SNPs.

TABLE D.1
SNPs selected by ℓ_1 -penalized Cox regression: #1-#56

Rank	SNP ID	Chr ^A	Location	A1 ^B	A2 ^C	MAF ^D	Mapped genes	Sign ^E	Known ^F
1	rs4506565	10	114756041	A	T	0.238	TCF7L2	+	Yes
2	rs12243326	10	114788815	C	T	0.249	TCF7L2	+	Yes
3	rs16891982	5	33951693	G	C	0.215	SLC45A2	-	
4	rs12255372	10	114808902	T	G	0.215	TCF7L2	+	Yes
5	rs12913832	15	28365618	G	A	0.198	HERC2	-	
6	rs28777	5	33958959	C	A	0.223	SLC45A2	-	
7	rs1129038	15	28356859	C	T	0.343	HERC2	-	
8	rs35397	5	33951116	T	G	0.304	SLC45A2	-	
9	rs10787472	10	114781297	C	A	0.430	TCF7L2	+	Yes
10	rs2470890	15	75047426	T	C	0.429	CYP1A2	-	
11	rs2472304	15	75044238	A	G	0.460	CYP1A2	-	
12	rs1378942	15	75077367	A	C	0.401	CSK, MIR4513	-	
13	rs34862454	15	75101530	T	C	0.416	LMAN1L	-	
14	rs849335	7	28223990	C	T	0.406	JAZF1, JAZF1-AS1	-	Yes
15	rs864745	7	28180556	C	T	0.316	JAZF1	-	Yes
16	rs12785878	11	71167449	T	G	0.251	NADSYN1, DHCR7	-	
17	rs4944958	11	71168073	G	A	0.237	NADSYN1, DHCR7	-	
18	rs8042680	15	91521337	A	C	0.277	PRC1, PRC1-AS1, Y_RNA	+	
19	rs35414	5	33969628	T	C	0.188	SLC45A2	-	
20	rs1635852	7	28189411	T	C	0.423	JAZF1	-	
21	rs10962525	9	16659863	T	C	0.321	BNC2	+	
22	rs1446585	2	136407479	G	A	0.322	R3HDM1	+	
23	rs7570971	2	135837906	A	C	0.327	RAB3GAP1	+	
24	rs36074798	15	91518800	ACT	A	0.328	PRC1, PRC1-AS1, Y_RNA	+	Yes
25	rs10962612	9	16804167	G	T	0.088	BNC2	-	
26	rs10962612	2	135911422	T	C	0.097	RAB3GAP1, ZRANB3	+	
27	rs941444	17	17693891	C	G	0.073	RAI1	-	Yes
28	rs6769511	3	185530290	T	C	0.045	IGF2BP2	+	Yes
29	rs916977	15	28513364	T	C	0.044	HERC2	-	
30	rs35390	5	33955326	C	A	0.062	SLC45A2	-	
31	rs35391	5	33955673	T	C	0.374	SLC45A2	-	
32	rs1470579	3	185529080	A	C	0.436	IGF2BP2	+	Yes
33	rs2862954	10	101912064	T	C	0.488	ERLIN1	-	
34	rs2297174	9	16706557	A	G	0.346	BNC2	-	
35	rs1667394	15	28530182	T	C	0.274	HERC2	-	
36	rs12440952	15	74615292	G	A	0.279	CCDC33	+	
37	rs56343038	9	16776792	G	T	0.318	BNC2, LSM1P1	-	
38	rs9522149	13	111827167	T	C	0.395	ARHGEF7	-	
39	rs343092	12	66250940	T	G	0.463	HMGA2, HMGA2-AS1	-	Yes
40	rs10733316	9	16696626	T	C	0.436	BNC2	-	
41	rs823485	1	234671267	T	C	0.488	LINC01354	+	
42	rs12910825	15	91511260	A	G	0.384	PRC1, PRC1-AS1, RCCD1	+	Yes
43	rs2959005	15	74618128	T	C	0.222	CCDC33	-	
44	rs10756801	9	16740110	T	G	0.494	BNC2	-	
45	rs12072073	1	3130016	C	T	0.497	PRDM16	+	
46	rs7039444	9	20253425	T	C	0.360	(intergenic variant)	+	
47	rs7899137	10	76668462	A	C	0.289	KAT6B	-	
48	rs11078405	17	17824978	T	G	0.291	TOM1L2	+	
49	rs830532	5	142289541	C	T	0.333	ARHGAP26	+	
50	rs833283	3	181590598	G	C	0.352	(intergenic variant)	-	
51	rs10274928	7	28142088	A	G	0.365	JAZF1	-	Yes
52	rs13301628	9	16665850	A	C	0.412	BNC2	-	
53	rs885107	16	30672719	C	T	0.353	PRR14, FBRS	+	
54	rs8180897	8	121699907	A	G	0.445	SNTB1	+	
55	rs23282	5	142270301	G	A	0.225	ARHGAP26	+	
56	rs6428460	1	198377460	C	T	0.229	(intergenic variant)	+	

^A Chromosome, ^B Minor allele, ^C Major allele, ^D Minor allele frequency,

^E Sign of the regression coefficient, ^F Mapped gene included in [Mahajan et al. \(2018\)](#). The boldface indicates the risk allele determined by the reference allele and the sign of the regression coefficient.

TABLE D.2
SNPs selected by ℓ_1 -penalized Cox regression: #57-#111

Rank	SNP ID	Chr ^A	Location	A1 ^B	A2 ^C	MAF ^D	Mapped genes	Sign ^E	Known ^F
57	rs11630918	15	75155896	C	T	0.383	SCAMP2	-	
58	rs7187359	16	30703155	G	A	0.335	(intergenic variant)	+	
59	rs2183405	9	16661933	G	A	0.271	BNC2	+	
60	rs2651888	1	3143384	G	T	0.411	PRDM16	+	
61	rs2189965	7	28172014	T	C	0.340	JAZF1	+	Yes
62	rs12911254	15	75166335	A	G	0.344	SCAMP2	-	
63	rs757729	7	28146305	G	C	0.441	JAZF1	-	Yes
64	rs6495122	15	75125645	C	A	0.478	CPLX3, ULK3	-	
65	rs4944044	11	71120213	A	G	0.426	AP002387.1	-	
66	rs6856032	4	38763994	G	C	0.109	RNA5SP158	+	
67	rs1375132	2	135954405	G	A	0.478	ZRANB3	+	
68	rs2451138	8	119238473	T	C	0.314	SAMD12	-	
69	rs6430538	2	135539967	T	C	0.470	CCNT2-AS1	+	
70	rs7651090	3	185513392	G	A	0.281	IGF2BP2	+	Yes
71	rs4918711	10	113850019	T	C	0.285	(intergenic variant)	-	
72	rs3861922	1	198210570	A	G	0.466	NEK7	+	
73	rs7917983	10	114732882	T	C	0.481	TCF7L2	+	Yes
74	rs1781145	1	1388289	A	C	0.362	ATAD3C	+	
75	rs7170174	15	94090333	T	C	0.246	AC091078.1	-	
76	rs7164916	15	91561446	T	C	0.246	VPS33B, VPS33B-DT	+	
77	rs696859	1	234656596	T	C	0.430	(intergenic variant)	+	
78	rs28052	5	142279870	C	G	0.166	ARHGAP26	+	
79	rs1408799	9	12672097	T	C	0.277	(intergenic variant)	-	
80	rs10941112	5	34004707	C	T	0.355	AMACR, C1QTNF3-AMACR	-	
81	rs11856835	15	74716174	G	A	0.261	SEMA7A	-	
82	rs4768617	12	45850022	T	C	0.259	(intergenic variant)	-	
83	rs8012970	14	101168491	T	C	0.179	(intergenic variant)	-	
84	rs4402960	3	185511687	G	T	0.187	IGF2BP2	+	Yes
85	rs1695824	1	1365570	A	C	0.164	LINC01770, VWA1	+	
86	rs934886	15	55939959	A	G	0.360	PRTG	-	
87	rs7083429	10	69303421	G	T	0.367	CTNNA3	+	
88	rs4918788	10	114820961	G	A	0.348	TCF7L2	+	Yes
89	rs7219320	17	17880877	A	G	0.318	DRC3, AC087163.1, ATPAF2	+	
90	rs61822626	1	205118441	C	T	0.478	DSTYK	-	Yes
91	rs250414	5	33990623	C	T	0.361	AMACR, C1QTNF3-AMACR	-	
92	rs11073964	15	91543761	C	T	0.362	VPS33B, PRC1	+	Yes
93	rs17729876	10	101999746	G	A	0.352	CWF19L1, SNORA12	-	
94	rs2386584	15	91539572	T	G	0.360	VPS33B, PRC1	+	Yes
95	rs683	9	12709305	C	A	0.430	TYRP1, LURAP1L-AS1	-	
96	rs17344537	1	205091427	T	G	0.462	RBBP5	-	
97	rs10416717	19	13521528	A	G	0.470	CACNA1A	+	
98	rs2644590	1	156875107	C	A	0.453	PEAR1	-	
99	rs447923	5	142252257	T	C	0.384	ARHGAP26, ARHGAP26-AS1	+	
100	rs2842895	6	7106316	C	G	0.331	RREB1	-	Yes
101	rs231354	11	2706351	C	T	0.329	KCNQ1, KCNQ1OT1	+	Yes
102	rs4959424	6	7084857	T	G	0.410	(intergenic variant)	-	
103	rs2153271	9	16864521	T	C	0.411	BNC2	-	
104	rs12142199	1	1249187	A	G	0.398	INTS11, PUSL1, ACAP3, MIR6727	-	
105	rs2733833	9	12705095	T	G	0.272	TYRP1, LURAP1L-AS1	-	
106	rs1564782	15	74622678	A	G	0.283	CCDC33	-	
107	rs9268644	6	32408044	C	A	0.282	HLA-DRA	+	
108	rs271738	1	234662890	A	G	0.395	LINC01354	+	
109	rs12907898	15	75207872	T	C	0.391	COX5A	-	
110	rs146900823	3	149192851	GC	C	0.344	TM4SF4	-	
111	rs1635166	15	28539834	T	G	0.118	HERC2	-	

^A Chromosome, ^B Minor allele, ^C Major allele, ^D Minor allele frequency,

^E Sign of the regression coefficient, ^F Mapped gene included in Mahajan et al. (2018). The boldface indicates the risk allele determined by the reference allele and the sign of the regression coefficient.